

Robust neuronal dynamics in premotor cortex during motor planning

Nuo Li^{1*}, Kayvon Daie^{1*}, Karel Svoboda¹ & Shaul Druckmann¹

Neural activity maintains representations that bridge past and future events, often over many seconds. Network models can produce persistent and ramping activity, but the positive feedback that is critical for these slow dynamics can cause sensitivity to perturbations. Here we use electrophysiology and optogenetic perturbations in the mouse premotor cortex to probe the robustness of persistent neural representations during motor planning. We show that preparatory activity is remarkably robust to large-scale unilateral silencing: detailed neural dynamics that drive specific future movements were quickly and selectively restored by the network. Selectivity did not recover after bilateral silencing of the premotor cortex. Perturbations to one hemisphere are thus corrected by information from the other hemisphere. Corpus callosum bisections demonstrated that premotor cortex hemispheres can maintain preparatory activity independently. Redundancy across selectively coupled modules, as we observed in the premotor cortex, is a hallmark of robust control systems. Network models incorporating these principles show robustness that is consistent with data.

Neurons in frontal and parietal cortex show slow dynamics, including persistent and ramping activity, related to motor planning^{1–4}, action timing^{5,6}, working memory^{7–10} and decision making^{11–13}. Neurons have intrinsic time constants on the order of ten milliseconds¹⁴. Slow dynamics over seconds are presumably an emergent property of neural circuits, probably involving feedback drive¹⁵ (but also see refs 16, 17).

Network models can produce persistent and ramping activity, including integrators^{15,18–21} and trained recurrent networks^{22–24}. The amplification that prolongs the model network response may cause fragility to perturbations of activity²⁵. By contrast, biological systems are typically robust to internal and external perturbations^{26,27}.

Controlled transient perturbations can probe the mechanisms underlying the dynamics in neural networks^{13,25,28,29}. Deviations from normal activity patterns are related to network structure. For example, attractor-like models predict recovery of the attractor state with altered dynamics, whereas chaotic systems diverge over time²⁵. Comparison of perturbed dynamics and behaviour can reveal which elements of the original dynamics are necessary.

We measured behavioural and neural responses after transiently silencing parts of the mouse premotor cortex (anterior lateral motor cortex, ALM). ALM neurons in both hemispheres, which are coupled via callosal axons, exhibit persistent preparatory activity that predicts specific movement directions, seconds before the movement^{3,30}. We report that preparatory activity is robust to unilateral perturbations. Theoretical analyses suggest that premotor networks are organized into redundant modules.

Preparatory activity in ALM

Mice performed pole location discrimination with their whiskers^{3,30} (Fig. 1a). During a subsequent delay epoch (1.3–1.7 s), mice planned the upcoming response. An auditory ‘go’ cue (0.1 s) signalled the beginning of the response epoch, and mice reported pole position by licking one of two ports (posterior to lick right; anterior to lick left).

ALM is involved in planning directional licking^{3,30,31}. We recorded single units from the left ALM ($n = 1,012$ units from 12 mice; Methods) (Fig. 1b). Most ALM pyramidal neurons distinguished trial types (634 out of 890, $P < 0.05$, t -test; sample epoch, 176 out of 890; delay

epoch, 337 out of 890; response epoch, 493 out of 890; Methods) (Extended Data Fig. 1). Selectivity was defined as the spike rate difference between ‘lick left’ and ‘lick right’ trials. Individual ALM neurons exhibited diverse patterns of activity during different task epochs, including persistent activity and ramping activity during the delay epoch, similar to activity seen across the frontal cortex^{1,2,4,5,8–10,32,33}, parietal cortex^{6,12} and subcortical brain areas³⁴.

Preparatory activity after unilateral silencing

Models of persistent and ramping activity^{5,18,22–24,35–37} do not recover after transiently silencing comparably sized subsets of neurons (Fig. 1c and Extended Data Fig. 1f–i). We transiently silenced preparatory activity³ (Fig. 1a) (‘photoinhibition’; Extended Data Fig. 2 and Methods). The standard photostimulus was one laser spot³, silencing 58% of one ALM hemisphere (>80% reduction of activity, Methods) (Fig. 1b). Transient (duration, 0.5 s) unilateral photoinhibition of ALM up to the go cue (late delay) caused an ipsilateral response bias ($n = 5$ mice, $P < 0.01$, two-tailed t -test; Fig. 1d), similar in magnitude to photoinhibition over the entire delay epoch^{3,30} (Extended Data Fig. 3). By contrast, photoinhibition ending at least 0.3 s before the go cue produced minimal behavioural effects (middle delay, early delay; $P > 0.1$, two-tailed t -test).

ALM activity was abolished during photoinhibition (Fig. 1e) ($n = 6$ mice). After photoinhibition offset preparatory activity recovered. ALM neurons that normally exhibited ramping activity during the delay epoch accelerated their ramping after photoinhibition so that activity ‘caught up’ to reach the same level as in unperturbed trials (Fig. 1e, neurons 1 and 2). Recovery was not due to non-specific overshoots in spike rate after photoinhibition (that is, ‘rebound’). First, we used photostimuli optimized to minimize rebound³ (Extended Data Fig. 2c). Second, selectivity also recovered, so that activity reached the appropriate spike rate for each trial type. Finally, neurons that normally did not exhibit increasing ramps during the delay epoch also recovered their activity (Fig. 1e, neuron 3; Extended Data Fig. 4). Within 400 ms of photoinhibition, spike rates became indistinguishable from the unperturbed condition in 90% of the neurons; only 10% of neurons retained a sustained change in spike rate (Fig. 1f). ALM neurons recovered >80% of their selectivity relative to the unperturbed trials within 514 ms of photoinhibition (Fig. 1g).

¹Janelia Research Campus, Howard Hughes Medical Institute, Ashburn, Virginia 20147, USA.

*These authors contributed equally to this work.

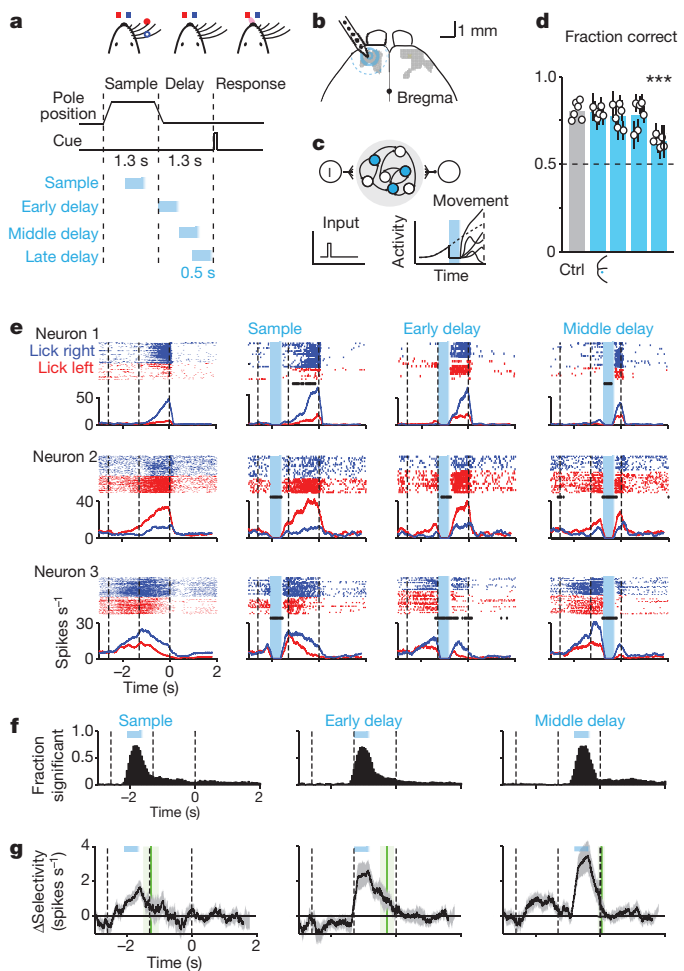


Figure 1 | ALM preparatory activity is robust to photooinhibition. **a**, Mice discriminate pole location during the sample epoch and respond ‘lick right’ or ‘lick left’ after a delay. Cyan, photooinhibition. **b**, Grey, ALM; area that produced behavioural effects with photooinhibition throughout the delay epoch (Methods; Allen Mouse Brain Atlas (<http://mouse.brain-map.org/static/atlas>)). Cyan, contours of photooinhibition (small, 90% reduction in activity; medium, 80%; large/dashed, 50%). **c**, Schematic network models and responses to transient photooinhibition of subsets of neurons (cyan). Dashed line, unperturbed activity trajectory; solid line, perturbed activity trajectory. **d**, Behavioural performance (see timing in **a**). Bar, mean. Symbols, individual mice (mean \pm s.e.m., bootstrap). Open circle, photooinhibition duration, 800 ms; solid triangle, 1,300 ms. *** $P < 0.001$, two-tailed t -test against control. **e**, Example neurons. Top, spike raster. Bottom, peristimulus time histogram (PSTH), averaged over 200 ms. Lick-right (blue) and lick-left (red) trials, grouped by instructed movement. Dashed lines, behavioural epochs. Cyan, photooinhibition. Black ticks above PSTH, significant spike rate change ($P < 0.01$, two-tailed t -test). **f**, Fraction of neurons with significant spike rate change ($n = 168, 168$ and 175). Cyan, photooinhibition. **g**, Δ Selectivity from control (mean \pm s.e.m. across neurons, bootstrap; selective neurons tested for >3 trials in all conditions, $n = 55$). Green lines, recovery to 80% of control (mean \pm s.e.m. bootstrap). Sample, 373 ± 260 ms; early delay, 510 ± 218 ms; middle delay, 327 ± 112 ms.

In separate experiments, we transiently (500 ms) photostimulated a subset of layer 5 pyramidal neurons³⁰ (Extended Data Fig. 5). After photostimulus offset, ALM activity and selectivity recovered with a time-course that was similar to recovery after photooinhibition. Thus, ALM premotor activity is robust to large perturbations of activity.

Preparatory activity after bilateral silencing

Perturbed ALM probably inherits preparatory activity from a connected area. ALM is bilaterally connected through the corpus callosum, and preparatory activity is found in both hemispheres³⁰. We

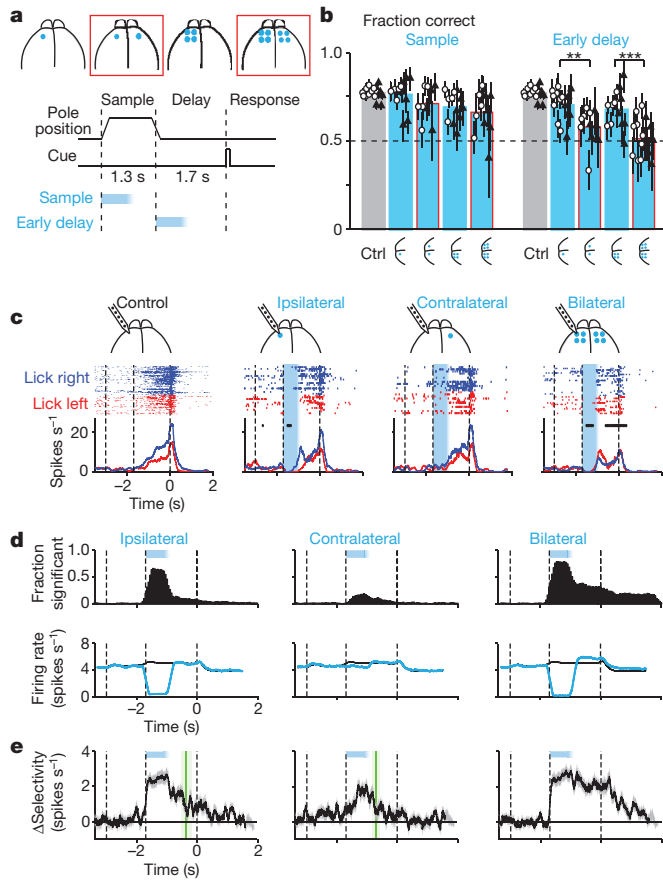


Figure 2 | Bilateral photooinhibition disrupts preparatory activity.

a, Unilateral and bilateral (red) photooinhibition. **b**, Behavioural performance. Bar, mean. Symbols, individual mice (mean \pm s.e.m., bootstrap). Open circle, photooinhibition duration, 800 ms; solid triangle, 1,300 ms. ** $P < 0.01$, *** $P < 0.001$, two-tailed t -test against control. **c**, Example ALM neuron. Cyan, photooinhibition. **d**, Fraction of neurons with significant spike rate change ($n = 276, 283$ and 332). Bottom, average spike rate across the population (black, control; cyan, photooinhibition). **e**, Average change in population selectivity from control ($n = 143$). Same as Fig. 1g. Selectivity recovery: ipsilateral, 538 ± 178 ms; contralateral, 192 ± 114 ms; bilateral, no recovery.

tested for coupling between hemispheres by silencing ALM activity either unilaterally or bilaterally ($n = 13$ mice) (Fig. 2a; Methods), using four protocols: (1) unilateral photooinhibition with one laser spot (left or right hemisphere); (2) bilateral photooinhibition using one spot on each side; (3) unilateral photooinhibition using a grid of four spots (1-mm spacing), silencing all of ALM and surrounding regions (Fig. 1b); and (4) bilateral photooinhibition using four spots on each side. Photooinhibition (duration 0.8 s or 1.3 s) was deployed during either the sample or early in the delay epoch, ending at least 0.4 s before the response cue (Fig. 2a).

Behavioural performance was only slightly affected after unilateral photooinhibition with a single spot during the early delay epoch (Fig. 2b, 70.3% correct, $P = 0.009$, two-tailed t -test against control); unilateral photooinhibition with four spots had a small additional effect (67.7%, $P = 0.003$). By contrast, using only two spots across both hemispheres caused performance to degrade severely (Fig. 2b, 58.0%, $P < 0.001$; difference from four spot unilateral: $P < 0.05$, two-tailed t -test); four spots bilaterally further reduced performance to near chance level (four laser spots: 51.4%, $P < 0.001$). This implies that the larger effects of bilateral photooinhibition were not simply due to the strength of photooinhibition. Bilateral photooinhibition biased movements inconsistently across mice and sessions (Extended Data Fig. 6a); we use this feature later to explore the relationship between ALM population dynamics and movement.

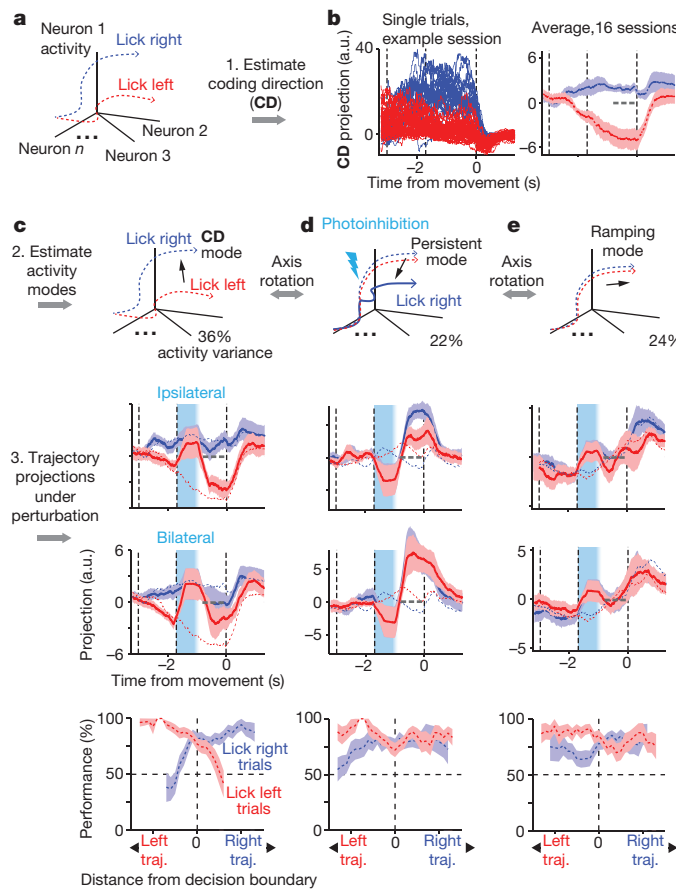


Figure 3 | Preparatory activity preferentially recovers along coding dimension in activity space. **a**, Schematic, movement-specific trajectories in activity space. **b**, Left, activity on correct lick-right (blue) and lick-left (red) trials projected onto the coding direction (CD). One session, 12 neurons. Right, average trajectories from all sessions (\pm s.e.m. bootstrap, Methods). All unperturbed trials (correct and incorrect), grouped by instructed movement. Dotted grey line, decision boundary. Averaging window, 400 ms. **c**, Top, illustration of the CD mode. Middle, activity in ipsilateral and bilateral photoinhibition trials projected onto the CD. All perturbed trials (correct and incorrect), grouped by instructed movement. Dashed blue and red lines, means for unperturbed trials (from **b**). Bottom, behavioural performance in lick-right (blue) and lick-left (red) trials as a function of trajectory distance from the decision boundary. Performance was computed by binning along the CD distance. s.e.m. was obtained by bootstrapping the trials in each bin. **d**, Same as in **c** for activity along persistent mode, which maximizes the difference between perturbed and unperturbed activity at the time of movement onset. This mode does not carry movement-specific information (middle; note that red and blue dashed lines are near each other) and does not predict movement direction (bottom). **e**, Same as **c** for population activity along the ramping mode, which explains most of the remaining activity variance (Methods). This mode shows robust ramping but is non-selective (middle) and does not predict movement direction (bottom).

We next recorded from left ALM during photoinhibition of left ALM (ipsilateral, one laser spot), right ALM (contralateral, one laser spot), and both hemispheres (four laser spots on each side) ($n=7$ mice). As before (Fig. 1), spike rate ($>90\%$) (Fig. 2c, d) and selectivity ($>80\%$) (Fig. 2e) recovered 600 ms after ipsilateral perturbation. ALM activity was hardly affected by contralateral photoinhibition (Fig. 2c, d and Extended Data Fig. 2e).

After bilateral photoinhibition, neurons recovered their spike rate on average (Fig. 2c, d), but selectivity failed to recover (Fig. 2c–e). Bilateral photoinhibition with one laser spot produced a larger persistent change in selectivity than unilateral photoinhibition with four laser spots (Extended Data Fig. 7). Recovery of selectivity after

unilateral photoinhibition was less robust with larger photoinhibition size (Extended Data Fig. 7e), similar to behaviour (Fig. 2b). Robustness to perturbation results from redundancy within the bilateral ALM network.

Robustness along the coding direction

Robust systems maintain critical functions in response to perturbations, whereas non-critical features may remain uncorrected²⁶. We analysed population dynamics in the activity space, in which each dimension corresponds to activity of one neuron (6–20 neurons recorded simultaneously; average, 11 neurons; 16 sessions)³⁸. Preparatory activity for different movements (lick-left versus lick-right) corresponded to distinct trajectories in the activity space (Fig. 3a).

We decomposed activity into several modes. First, we estimated the coding direction (CD) along which preparatory activity maximally discriminated upcoming directional licking (Methods, Fig. 3b). After ipsilateral photoinhibition the CD mode recovered to trajectories similar to the unperturbed trials (Fig. 3c; receiver operating characteristic (ROC) values between trajectories at the end of delay epoch: control, 0.76 ± 0.03 ; ipsilateral, 0.73 ± 0.02 ; mean \pm s.e.m. across sessions; Methods). Contralateral photoinhibition had little effect (Extended Data Fig. 8; ROC, 0.74 ± 0.03). As expected (Fig. 2), trajectories were permanently altered after bilateral photoinhibition, resulting in small separation between the trajectories for different trial types at the time of movement onset (ROC, 0.58 ± 0.03). We used a decision boundary, on the CD that separated the lick-left versus lick-right trials (Methods), to predict upcoming movement on a trial-by-trial basis. Deviations towards the lick-right trajectory predicted more frequent lick-right responses and vice versa (Fig. 3, Extended Data Fig. 8). Activity along the CD predicts trial type.

Second, we obtained a mode that maximized sustained effects of ipsilateral perturbations (persistent mode, Fig. 3d). By construction, the persistent mode was altered by the perturbation, up to and beyond movement onset. However, this projection did not discriminate trial type nor predict behaviour on control trials.

Third, a mode that maximally captured the remaining activity variance, showed non-selective ramping during the delay epoch, did not predict behaviour, and was resistant to unilateral and bilateral perturbations (Fig. 3e; see Extended Data Fig. 8 for a full decomposition of ALM dynamics). This ramping mode could reflect non-specific ‘urgency’³⁹ driven by a source external to ALM.

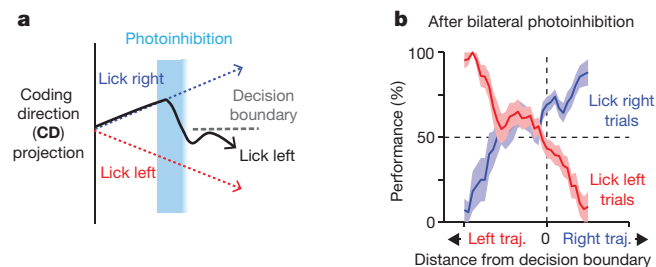
Preparatory activity is therefore maintained by ALM populations along specific trajectories in a sub-space of neural activity space. Circuit dynamics are actively restored along behaviour-related directions in the activity space, but not along certain non-informative directions^{33,40}.

We next examined ALM population activity after bilateral perturbation and its relationship to behaviour. Individual trials with a deviation towards the lick-right trajectory along the CD predicted more frequent lick-right responses and vice versa (Fig. 4, Extended Data Figs 6b and 9). This analysis shows that even after average selectivity is destroyed by perturbations, ALM population dynamics still dictate upcoming movements.

Contralateral input is required for recovery

Preparatory activity is coupled across the two ALM hemispheres (Figs 2 and 3). The small effect seen on activity with contralateral inhibition (Extended Data Figs 2e and 8d) suggests further that ALM hemispheres function as modules, maintaining preparatory activity independently²⁸. After unilateral perturbation, information from the unperturbed side helps to recover the function of the perturbed side. To test directly the role of contralateral ALM input as the corrective signal, we bisected the ALM corpus callosum ($n=7$ mice) (Fig. 5a, Methods), sparing pyramidal tract and corticothalamic axons (Extended Data Fig. 10).

Notably, behavioural performance was unaffected (Fig. 5b, control trials, before versus after callosotomy, $P > 0.05$, two-tailed *t*-test), with normal performance 17 h after callosotomy (Extended Data Fig. 10b).



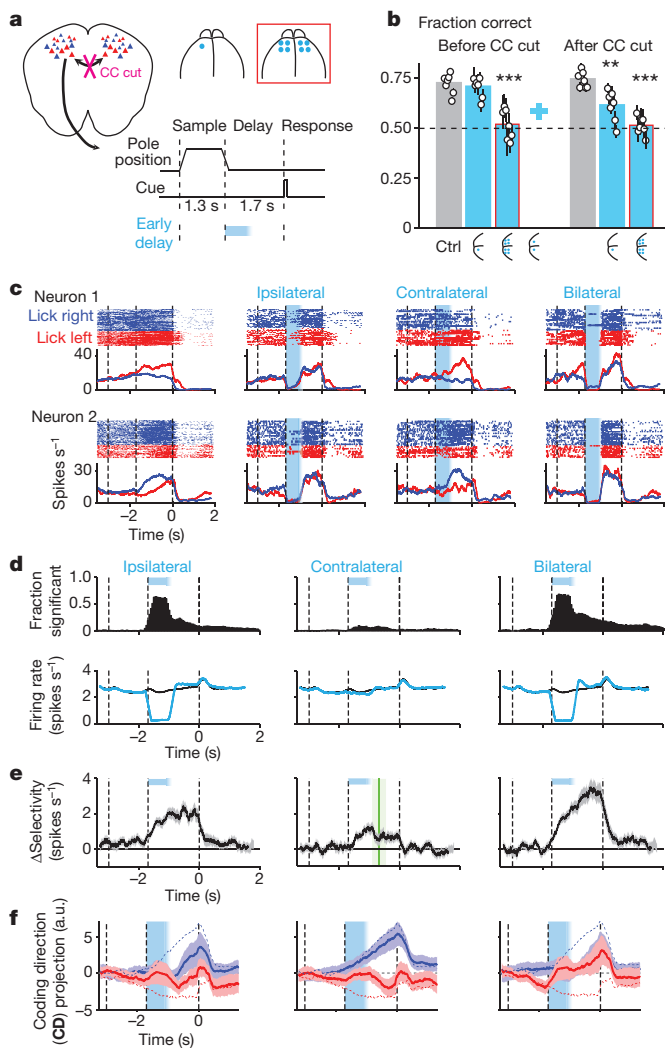
However, behavioural performance was now highly sensitive to transient unilateral photooinhibition (Fig. 2b, 1 laser spot: $P = 0.0019$, two-tailed t -test against control). There was a significant interaction between callosotomy and unilateral photooinhibition ($P = 0.0035$, repeated measure two-way analysis of variance, ANOVA). Behavioural performance after unilateral photooinhibition dropped to the same level as bilateral photooinhibition in control mice (Fig. 5b, blue cross).

Preparatory activity in callosotomized mice ($n = 7$ mice) was similar to control mice (Fig. 5c and Extended Data Fig. 10), providing additional evidence that the two ALM hemispheres can maintain preparatory activity independently. After ipsilateral photooinhibition, ALM neurons recovered their average spike rate (Fig. 5c, d), but selectivity failed to recover (Fig. 5e). Selectivity in the coding direction was reduced (Fig. 5f, 16 sessions). Preparatory activity is distributed redundantly across interacting modules in the two ALM hemispheres.

Robust model networks

We compared ALM population dynamics under perturbations (Figs 1 and 2) to predictions from network models (Extended Data Fig. 1). After ipsilateral photooinhibition, ALM activity rapidly recovered to the unperturbed trajectory (Figs 1 and 3). This is inconsistent with attractors with a pair of fixed points (one for each choice condition)²⁹. After release from perturbation, these models decay to the final fixed point and do not return to the trajectory (Extended Data Fig. 4c). Integrator models with a continuum of fixed points generate ramping activity by integrating their inputs^{5,28,37}; these models predict an activity offset compared to the unperturbed trajectories, inconsistent with the data (Extended Data Fig. 1f, g). We also tested randomly connected recurrent networks trained to produce ramping triggered by a transient input^{22–24} (trained random recurrent networks, RRNs). These models failed to recover from perturbations (Extended Data Fig. 1h, i). Overall, all monolithic models consisting of one network were unable to explain robustness.

Preparatory activity is distributed across modules in both ALM hemispheres (Figs 2, 3 and 5). We therefore explored models with the following organizational principles (Fig. 6a): each module can produce ramping independently; recovery from unilateral perturbation is achieved by specific inter-module connectivity (for example, commissural axons); the inter-module connections have little net effect during normal operation. Figure 6b shows a model comprised of two identical modules (corresponding to hemispheres), each consisting of a pair of identical units that inhibit each other and excite themselves to produce ramping activity towards one of two fixed points (representing lick-right or lick-left movements; Methods). Selective commissural connections restored activity on the other side after unilateral transient silencing (Fig. 6b). When the two sides are silenced, the network drifts to one of the fixed points randomly. Similar schemes allowed the integrator and trained RRN to be adapted into a modular and redundant architecture that is robust to unilateral perturbations (Fig. 6c, d; Methods). Imposing modular architecture upon any monolithic model



allowed it to reproduce the stability found in the data, suggesting the modular architecture itself, and not any particular detail of the models, as the key factor in robustness.

Discussion

Our neurophysiological and behavioural analysis of preparatory activity provides three insights. First, preparatory activity is robust to large, transient perturbations of the network (Fig. 1). Second, unperfused parts of the network remain functional during the perturbation and help the perturbed part of the network to recover after the perturbation (Figs 2 and 5). Third, premotor cortex preparatory activity recovers in dimensions relevant to behaviour and less so in other dimensions (Fig. 3). This indicates that premotor networks are organized into functionally segregated modules that interact selectively depending on their mutual state (Fig. 6).

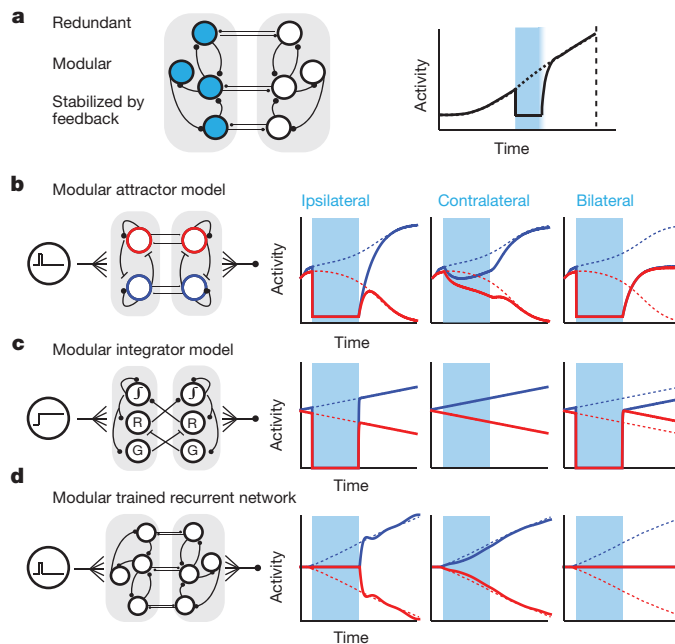


Figure 6 | Modular network models of premotor dynamics. **a**, Schematic, a modular network robust to transient photoinhibition of one module. **b**, Modular attractor model. Neurons with right (blue) and left (red) preferences provide self-excitation and mutual inhibition. Connections between modules involve neurons with similar preference. See Methods for model parameters in **b–d**. **c**, Modular integrator model¹⁵. Connections between modules restore activity on other side ('recovery' neurons, R). Gating (G) neurons cancel the inter-module coupling during normal operation. **d**, Modular recurrent network trained with FORCE learning²² to recapitulate single hemisphere perturbation.

ALM is involved in both planning and driving movements³⁰. Consistent with this view, unilateral photoinhibition of ALM late in the delay epoch abolished the contralateral motor command, resulting in ipsilateral bias (Fig. 1 and Extended Data Fig. 3); furthermore, bilateral photoinhibition during the early delay epoch abolished the motor plan and scrambled future movements (Fig. 2). Previous optogenetic inactivation studies focusing on related brain areas have interpreted a lack of effect of transient inactivation as a lack of role in behaviour^{13,42}. Our results suggest that redundancy across a distributed network could mask possible causal roles in optogenetics experiments.

Modular architecture and functional redundancy are key components of robust engineered systems²⁶. Similarly, our data and previous experiments^{3,30} imply that the cortical networks maintaining motor plans are organized in a redundant and modular fashion. When ALM is silenced in one hemisphere, preparatory activity in the other hemisphere is weakly affected (Fig. 2 and Extended Data Figs 2e and 8d). However, after the perturbation, activity in the unperturbed hemisphere is critical to restore the perturbed preparatory activity in the opposite hemisphere. Preparatory activity is thus distributed in a redundant fashion across functional modules that can both operate independently and correct each other. The cortical networks involved in working memory could be organized in a similar manner^{7–10}. It is likely that modularity and redundancy operate in circuits contained in one hemisphere, perhaps even spatially interdigitated.

The responses of ALM neurons to perturbations can be decomposed into three types of dynamics: modes that are rapidly restored after unilateral perturbation; modes that remain perturbed; and modes that are restored both for unilateral and bilateral perturbation and are thus likely to be driven externally. Only behaviour-relevant modes recovered quickly. ALM responses to perturbations resemble robust systems, in which critical state variables are particularly stiff²⁶. Selective stability of neural dynamics supports the idea that behaviour-related activity

comprises only a low-dimensional subspace of neural activity space^{33,40}, constrained by the structure of neural circuits⁴³. Our findings place constraints on the circuit architectures that underlie memory-related cortical activity and suggest general principles of robust system control in the brain.

Online Content Methods, along with any additional Extended Data display items and Source Data, are available in the online version of the paper; references unique to these sections appear only in the online paper.

Received 13 October 2015; accepted 8 March 2016.

Published online 13 April 2016.

- Tanji, J. & Evarts, E. V. Anticipatory activity of motor cortex neurons in relation to direction of an intended movement. *J. Neurophysiol.* **39**, 1062–1068 (1976).
- Churchland, M. M., Cunningham, J. P., Kaufman, M. T., Ryu, S. I. & Shenoy, K. V. Cortical preparatory activity: representation of movement or first cog in a dynamical machine? *Neuron* **68**, 387–400 (2010).
- Guo, Z. V. et al. Flow of cortical activity underlying a tactile decision in mice. *Neuron* **81**, 179–194 (2014).
- Erlich, J. C., Bialek, M. & Brody, C. D. A cortical substrate for memory-guided orienting in the rat. *Neuron* **72**, 330–343 (2011).
- Murakami, M., Vicente, M. I., Costa, G. M. & Mainen, Z. F. Neural antecedents of self-initiated actions in secondary motor cortex. *Nature Neurosci.* **17**, 1574–1582 (2014).
- Maimon, G. & Assad, J. A. A cognitive signal for the proactive timing of action in macaque LIP. *Nature Neurosci.* **9**, 948–955 (2006).
- Fuster, J. M. & Alexander, G. E. Neuron activity related to short-term memory. *Science* **173**, 652–654 (1971).
- Funahashi, S., Bruce, C. J. & Goldman-Rakic, P. S. Mnemonic coding of visual space in the monkey's dorsolateral prefrontal cortex. *J. Neurophysiol.* **61**, 331–349 (1989).
- Romo, R., Brody, C. D., Hernandez, A. & Lleras, L. Neuronal correlates of parametric working memory in the prefrontal cortex. *Nature* **399**, 470–473 (1999).
- Liu, D. et al. Medial prefrontal activity during delay period contributes to learning of a working memory task. *Science* **346**, 458–463 (2014).
- Wang, X. J. Decision making in recurrent neuronal circuits. *Neuron* **60**, 215–234 (2008).
- Gold, J. I. & Shadlen, M. N. The neural basis of decision making. *Annu. Rev. Neurosci.* **30**, 535–574 (2007).
- Hanks, T. D. et al. Distinct relationships of parietal and prefrontal cortices to evidence accumulation. *Nature* **520**, 220–223 (2015).
- Mainen, Z. F. & Sejnowski, T. J. Reliability of spike timing in neocortical neurons. *Science* **268**, 1503–1506 (1995).
- Cannon, S. C., Robinson, D. A. & Shamma, S. A proposed neural network for the integrator of the oculomotor system. *Biol. Cybern.* **49**, 127–136 (1983).
- Sheffield, M. E., Best, T. K., Mensh, B. D., Kath, W. L. & Spruston, N. Slow integration leads to persistent action potential firing in distal axons of coupled interneurons. *Nature Neurosci.* **14**, 200–207 (2011).
- Yoshida, M. & Hasselmo, M. E. Persistent firing supported by an intrinsic cellular mechanism in a component of the head direction system. *J. Neurosci.* **29**, 4945–4952 (2009).
- Barak, O., Sussillo, D., Romo, R., Tsodyks, M. & Abbott, L. F. From fixed points to chaos: three models of delayed discrimination. *Prog. Neurobiol.* **103**, 214–222 (2013).
- Murakami, M. & Mainen, Z. F. Preparing and selecting actions with neural populations: toward cortical circuit mechanisms. *Curr. Opin. Neurobiol.* **33**, 40–46 (2015).
- Fisher, D., Olasagasti, I., Tank, D. W., Aksay, E. R. & Goldman, M. S. A modeling framework for deriving the structural and functional architecture of a short-term memory microcircuit. *Neuron* **79**, 987–1000 (2013).
- Wang, X. J. Synaptic reverberation underlying mnemonic persistent activity. *Trends Neurosci.* **24**, 455–463 (2001).
- Sussillo, D. & Abbott, L. F. Generating coherent patterns of activity from chaotic neural networks. *Neuron* **63**, 544–557 (2009).
- Laje, R. & Buonomano, D. V. Robust timing and motor patterns by taming chaos in recurrent neural networks. *Nature Neurosci.* **16**, 925–933 (2013).
- Mante, V., Sussillo, D., Shenoy, K. V. & Newsome, W. T. Context-dependent computation by recurrent dynamics in prefrontal cortex. *Nature* **503**, 78–84 (2013).
- London, M., Roth, A., Beeren, L., Häusser, M. & Latham, P. E. Sensitivity to perturbations *in vivo* implies high noise and suggests rate coding in cortex. *Nature* **466**, 123–127 (2010).
- Kitano, H. Biological robustness. *Nature Rev. Genet.* **5**, 826–837 (2004).
- Csete, M. E. & Doyle, J. C. Reverse engineering of biological complexity. *Science* **295**, 1664–1669 (2002).
- Aksay, E. et al. Functional dissection of circuitry in a neural integrator. *Nature Neurosci.* **10**, 494–504 (2007).
- Kopec, C. D., Erlich, J. C., Brunton, B. W., Deisseroth, K. & Brody, C. D. Cortical and subcortical contributions to short-term memory for orienting movements. *Neuron* **88**, 367–377 (2015).
- Li, N., Chen, T. W., Guo, Z. V., Gerfen, C. R. & Svoboda, K. A motor cortex circuit for motor planning and movement. *Nature* **519**, 51–56 (2015).

31. Komiyama, T. *et al.* Learning-related fine-scale specificity imaged in motor cortex circuits of behaving mice. *Nature* **464**, 1182–1186 (2010).
32. Shenoy, K. V., Sahani, M. & Churchland, M. M. Cortical control of arm movements: a dynamical systems perspective. *Annu. Rev. Neurosci.* **36**, 337–359 (2013).
33. Kaufman, M. T., Churchland, M. M., Ryu, S. I. & Shenoy, K. V. Cortical activity in the null space: permitting preparation without movement. *Nature Neurosci.* **17**, 440–448 (2014).
34. Tanaka, M. Cognitive signals in the primate motor thalamus predict saccade timing. *J. Neurosci.* **27**, 12109–12118 (2007).
35. Seung, H. S. How the brain keeps the eyes still. *Proc. Natl Acad. Sci. USA* **93**, 13339–13344 (1996).
36. Amit, D. J. & Brunel, N. Model of global spontaneous activity and local structured activity during delay periods in the cerebral cortex. *Cereb. Cortex* **7**, 237–252 (1997).
37. Lim, S. & Goldman, M. S. Balanced cortical microcircuitry for maintaining information in working memory. *Nature Neurosci.* **16**, 1306–1314 (2013).
38. Stopfer, M., Jayaraman, V. & Laurent, G. Intensity versus identity coding in an olfactory system. *Neuron* **39**, 991–1004 (2003).
39. Cisek, P., Puskas, G. A. & El-Murr, S. Decisions in changing conditions: the urgency-gating model. *J. Neurosci.* **29**, 11560–11571 (2009).
40. Druckmann, S. & Chklovskii, D. B. Neuronal circuits underlying persistent representations despite time varying activity. *Curr. Biol.* **22**, 2095–2103 (2012).
41. Goldman, M. S. Memory without feedback in a neural network. *Neuron* **61**, 621–634 (2009).
42. Diester, I. *et al.* An optogenetic toolbox designed for primates. *Nature Neurosci.* **14**, 387–397 (2011).
43. Sadtler, P. T. *et al.* Neural constraints on learning. *Nature* **512**, 423–426 (2014).

Acknowledgements We thank B. DePasquale, A. Finkelstein, D. Gutnisky, A. Hantman, H. Inagaki, V. Jayaraman, J. Magee, S. Peron, S. Romani and N. Spruston for comments on the manuscript and discussion, T. Pluntke for animal training, A. Hu for histology, T. Harris and B. Barbarits for silicon probe recording system. This work was funded by Howard Hughes Medical Institute. N.L. and K.D. are Helen Hay Whitney Foundation postdoctoral fellows.

Author Contributions N.L., K.S. and S.D. conceived and designed the experiments. N.L. and K.D. performed behavioural experiments. N.L. performed electrophysiology and optogenetic experiments. K.D. and S.D. performed modeling. N.L., K.D., K.S. and S.D. analysed data and wrote the paper.

Author Information Data have been deposited at the CRCNS (<https://crcns.org/>) and can be accessed at <http://dx.doi.org/10.6080/KORB72JW>. Reprints and permissions information is available at www.nature.com/reprints. The authors declare no competing financial interests. Readers are welcome to comment on the online version of the paper. Correspondence and requests for materials should be addressed to K.S. (svobodak@janelia.hhmi.org) or S.D. (druckmanns@janelia.hhmi.org).

METHODS

Mice. This study is based on data from 33 mice (both males and females, age >postnatal day (P) 60). Ten VGAT-ChR2-EYFP mice (Jackson Laboratory, JAX 014548) and nine PV-ires-cre⁴⁴ crossed to Rosa26-LSL-ReaChR, red-shifted channelrhodopsin reporter mice (JAX 24846)⁴⁵, were used for photoinhibition behaviour experiments. A subset of these mice (five VGAT-ChR2-EYFP mice, seven PV × ReaChR mice) was used for simultaneous electrophysiology and behaviour. Seven mice (six VGAT-ChR2-EYFP, one PV × ReaChR mice) were used for the callosotomy experiment. Two Tlx_PL56-cre (MMRRC 036547)⁴⁶ crossed to Ai32 (Rosa26-ChR2 reporter mice, JAX 012569)⁴⁷ mice were used for photoactivation experiment. Two untrained VGAT-ChR2-EYFP mice and two untrained PV × ReaChR mice were used to characterize the photoinhibition in ALM. One Tlx_PL56-cre mouse was used for anatomical characterization of the ALM axonal projection pattern.

All procedures were in accordance with protocols approved by the Janelia Institutional Animal Care and Use Committee. Mice were housed in a 12 h:12 h reverse light:dark cycle and tested during the dark phase. On days not tested, mice received 1 ml of water. On other days, mice were tested in experimental sessions lasting 1–2 h, in which they received all their water (range, 0.5–2 ml). If mice did not maintain a stable body weight, they received supplementary water⁴⁸. All surgical procedures were carried out aseptically under 1–2% isoflurane anaesthesia. Buprenorphine HCl (0.1 mg kg⁻¹, intraperitoneal injection; Bedford Laboratories) was used for postoperative analgesia. Ketoprofen (5 mg kg⁻¹, subcutaneous injection; Fort Dodge Animal Health) was used at the time of surgery and postoperatively to reduce inflammation. After the surgery, mice were allowed to recover for at least 3 days with free access to water before water restriction.

The experiments were not randomized. The investigators were not blinded to allocation during experiments and outcome assessment.

Behaviour and surgery. Mice were prepared for photoinhibition and electrophysiology with a clear-skull cap and a headpost³. The scalp and periosteum over the dorsal surface of the skull were removed. A layer of cyanoacrylate adhesive (Krazy glue, Elmer's Products Inc.) was directly applied to the intact skull. A custom made headpost⁴⁸ was placed on the skull with its anterior edge aligned with the suture lambda (approximately over cerebellum) and cemented in place with clear dental acrylic (Lang Dental Jet Repair Acrylic; 1223-clear). A thin layer of clear dental acrylic was applied over the cyanoacrylate adhesive covering the entire exposed skull, followed by a thin layer of clear nail polish (Electron Microscopy Sciences, 72180).

The behavioural task and training have been described^{3,48}. The stimulus was a metal pin (0.9 mm in diameter), presented at one of two possible positions (Fig. 1a). The two pole positions were 4.29 mm apart along the anterior-posterior axis (approximately 40° of whisking angle) and were constant across sessions. The posterior pole position was 5 mm from the whisker pad. A two-spout lickport (4.5 mm between spouts) was used to record answer licks and deliver water rewards.

At the beginning of each trial, the vertical pole moved into reach of the whiskers (0.2 s travel time), where it remained for 1 s, after which it was retracted (retraction time 0.2 s). The sample epoch is defined as the time between the pole movement onset to 0.1 s after the pole retraction onset (sample epoch, 1.3 s, Fig. 1a). Mice touched the object at both pole positions, typically with a different set of whiskers. The delay epoch (durations, 1.2–1.7 s) followed the sample epoch. An auditory ‘go’ cue indicated the end of the delay epoch (pure tone, 3.4 kHz, 0.1 s duration). Licking early during the trial was punished by a loud alarm sound (siren buzzer, 0.05 s duration), followed by a brief timeout (1–1.2 s). Licking the correct lickport after the go cue led to a liquid reward (3 µl). Licking the incorrect lickport triggered a timeout (2–5 s). Trials in which mice did not lick within a 1.5-s window after the go cue were rare and typically occurred at the end of a session.

Photoinhibition. Light from a 473 nm laser (Laser Quantum, Gem 473) or a 594 nm laser (Cobolt Inc., Cobolt Mambo 100) was controlled by an acousto-optical modulator (AOM; Quanta Tech) and a shutter (Vincent Associates). Photoinhibition of ALM was performed through the clear-skull cap implant by directing the laser over the skull (beam diameter: 400 µm at 4σ). The light transmission through the intact skull is 50%³. Photoinhibition was deployed on 25% of the behavioural trials during behavioural testing. To prevent the mice from distinguishing photoinhibition trials from control trials using visual cues, a ‘masking flash’ (40 1-ms pulses at 10 Hz) was delivered using 470 nm or 591 nm LEDs (Luxeon Star) near the eyes of the mice. The masking flash began as the pole started to move and continued through the end of photoinhibition. For silencing we stimulated cortical GABAergic neurons in VGAT-ChR2-EYFP mice, or parvalbumin-positive interneurons in PV-ires-cre mice crossed to reporter mice expressing ReaChR⁴⁵. The two methods resulted in similar photoinhibition (Extended Data Fig. 2). The photoinhibition silenced 90% of spikes (Extended Data Fig. 2b) in a cortical area of 1 mm radius (at half-max) through all cortical layers³ (Extended

Data Fig. 2d). To minimize rebound excitation after photoinhibition offset, we linearly ramped down the laser power (100 or 200 ms). This photostimulus was empirically determined³ to produce robust photoinhibition with minimal rebound (Extended Data Fig. 2c).

The duration of the delay epoch varied to accommodate different photoinhibition conditions. In the unilateral photoinhibition experiment (Fig. 1, Extended Data Fig. 2a), a fixed 1.3-s delay epoch was used. We used a 40-Hz photostimulus with a sinusoidal temporal profile (1.5 mW average power) and a 100-ms linear ramp. We photoinhibited for 0.5 s, including the 100 ms ramp, during different task epochs (Fig. 1a). Photostimuli ended 1.6 s (sample), 0.8 s (early delay), 0.3 s (late delay), or 0 s (before cue) before the go cue. We also tested unilateral photoinhibition of longer durations in separate experiments (1.3 s including a 100-ms ramp, Extended Data Fig. 3). To accommodate the longer photoinhibition, we randomly varied the duration of the delay epoch from 1.2 s to 1.7 s in 0.1-s increments. This resulted in photoinhibition that terminated at different times before the go cue.

In the bilateral photoinhibition experiment (Fig. 2), a fixed 1.7-s delay epoch was used to allow more time for neuronal activity to recover after photoinhibition. We photoinhibited for 0.8 s, including a 200-ms ramp during offset, either at the beginning of the sample epoch or at the beginning of the delay epoch. To photoinhibit single cortical locations (Fig. 2a, 1 laser spot), we used the 40-Hz sinusoidal photostimulus (1.5 mW average power). To photoinhibit multiple cortical locations (Fig. 2a, multiple laser spots), we used a constant photostimulus and a scanning galvo (GVSM002, Thorlabs), which stepped the laser beam sequentially through the photoinhibition sites at the rate of 1 step per 5 ms (step time: <0.2 ms; dwell time: >4.8 ms; measured using a photodiode). Peak power was adjusted depending on the number of cortical locations to achieve 1.5 mW average power per location. The photoinhibition during scanning was similar to the standard condition (Extended Data Fig. 2).

To estimate the proportion of ALM silenced by photoinhibition, we estimated the boundaries of ALM using photoinhibition behavioural data from³. ALM was defined as the area where photoinhibition over the entire delay epoch produced significant behavioural effects. ALM boundaries (Fig. 1b, grey area) were derived by deconvolving the area producing significant behavioural effects with the point-spread function of the photoinhibition method³ (Extended Data Fig. 2d). At 80% activity reduction, photoinhibition with 1 laser spot covered 58% of ALM in one hemisphere (Fig. 1b).

Photoactivation. For photoactivation we stimulated layer 5 intratelencephalic neurons in Tlx_PL56-cre mice⁴⁶ crossed to reporter mice expressing ChR2 (Ai32)³⁰. The delay epoch was 1.3 s long. The photostimulus was a 20-Hz sinusoid (0.53 mW average power) applied during different task epochs (Extended Data Fig. 5b). Photoactivation was deployed on 40% of the behavioural trials during electrophysiology.

Electrophysiology. A small craniotomy (diameter, 1 mm) was made over left ALM (centred on 2.5 mm anterior, 1.5 mm lateral) one day before the recording session³. Extracellular spikes were recorded using NeuroNexus silicon probes (A4x8-5 mm-100-200-177). The 32 channel voltage signals were multiplexed, digitized by a PCI6133 board at 312.5 kHz (National instrument) at 14 bit, demultiplexed (sampling at 19531.25 Hz) and stored for offline analysis. Three to seven recordings were made from each craniotomy. To minimize brain movement, a drop of silicone gel (3-4680, Dow Corning) was applied over the craniotomy after the electrode was in the tissue. The tissue was allowed to settle for several minutes before the recording started.

During electrophysiology, photoinhibition was deployed on 40% of the trials to obtain a larger number of trials per condition. Three photoinhibition conditions were tested during each recording session. In the unilateral photoinhibition experiment (Fig. 1, Extended Data Fig. 2a), photoinhibition during sample, early delay, and late delay epoch were tested. In the bilateral photoinhibition experiment (Fig. 2, Extended Data Fig. 2a), photoinhibition of left ALM (ipsilateral, 1 laser spot), right ALM (contralateral, 1 laser spot), and both hemispheres (4 laser spot) were tested. In separate experiments (Extended Data Figs 2a and 7), ipsilateral photoinhibition with 4 laser spots, contralateral photoinhibition with 4 laser spots, and bilateral photoinhibition with 1 laser spot were tested.

Callosotomy. The placement of the corpus callosum cut was determined based on ALM axonal projection patterns. AAV2/1-CAG-EGFP (Addgene, plasmid 28014) was injected into one hemisphere of ALM (Extended Data Fig. 10c). The injection coordinate was 2.5 mm anterior to bregma and 1.5 mm lateral to the midline. The injection was made through the thinned skull using a custom volumetric injection system. Glass pipettes (Drummond) were pulled and bevelled to a sharp tip (outer diameter of 30 µm). Pipettes were back-filled with mineral oil and front-loaded with viral suspension immediately before injection. 50-nl volumes were injected 500 and 800 µm deep. Two weeks after injection, mice were perfused and their brains were sectioned (50 µm) and processed using standard

fluorescent immunohistochemical techniques. Confocal images were acquired on a Zeiss microscope, a $10 \times$ objective and a Hamamatsu Orca Flash 4 camera⁴⁶.

ALM axons extend caudally from the injection site. Corpus callosum axons separate from pyramidal tract and corticothalamic axons approximately 1.2 mm anterior to bregma. ALM corpus callosum axons were confined to the anterior regions of corpus callosum and were densest around 1 mm from bregma (Extended Data Fig. 10c). Corpus callosum axon bisection was made through an elongated craniotomy either over the left (3 mice) or right (4 mice) hemisphere. A 3.5-mm-deep cut was made using a micro knife (Fine Science Tools, 10318-14) mounted on a micromanipulator (Sutter Instrument). The cut was 0.5 mm from the midline and was at a slight angle to avoid the pyramidal tract and corticothalamic axons (Extended Data Fig. 10d). The cut extended from 1.5 mm anterior to bregma to 1 mm posterior. Care was taken to avoid damaging the superior sagittal sinus. In the same surgery, a second craniotomy was made over left ALM for electrophysiology. Approximately 17 h after the surgery mice were tested in behavioural experiments (Fig. 5, Extended Data Fig. 10). Mice were tested in daily recording sessions for 5–7 days after the callosotomy. Mice were perfused immediately after the last recording session and the brains were processed for histology (Extended Data Fig. 10d). In a subset of the mice, brain sections were stained for GFAP (mouse; Sigma G3893, 1:2,000 dilution) (Extended Data Fig. 10d).

Behavioural data analysis. Performance was computed as the fraction of correct reports, excluding lick-early trials (Figs 1–5). Chance performance was 50%. We also separately computed the performance for lick-right and lick-left trials (Figs 3, 4 and Extended Data Figs 3, 6, 9). Behavioural effects of photoinhibition were quantified by comparing the performance under photoinhibition with control performance using two-tailed *t*-test (Figs 1, 2, 5 and Extended Data Fig. 3).

Electrophysiology data analysis. The extracellular recording traces were band-pass filtered (300–6 kHz). Events that exceeded an amplitude threshold (4 s.d. of the background) were subjected to manual spike sorting to extract single units³. 1,012 single units were recorded during behaviour across 58 recording sessions (20 sessions of unilateral experiments, Fig. 1; 38 sessions of bilateral experiments, Fig. 2, Extended Data Fig. 7). Spike widths were computed as the trough-to-peak interval in the mean spike waveform. Units with spike width <0.35 ms were defined as fast-spiking neurons (72 out of 1,012) and units with spike widths >0.45 ms as putative pyramidal neurons (890 out of 1,012). Units with intermediate values (0.35–0.45 ms, 50 out of 1,012) were excluded. This classification was previously verified by optogenetic tagging of GABAergic neurons³. We concentrated our analyses on the putative pyramidal neurons.

Neurons were tested for significant trial-type selectivity during the sample, delay, or response epochs, using the spike counts from the lick-left and lick-right trials (two-tailed *t*-test, $P < 0.05$). Neurons that significantly differentiated trial types during any one of the trial epochs were deemed ‘selective’ (634 out of 890). To compute selectivity (Figs 1, 2, 5 and Extended Data Fig. 1), we first determined each neuron’s preferred trial type using spike counts from a subset of the trials (10 trials), selectivity is calculated as the spike rate difference between the trial types on the remaining data. Standard errors of the mean were obtained by bootstrap across neurons.

To quantify the effect of photoinhibition on individual ALM neuron spike rates (Figs 1, 2, 5 and Extended Data Figs 5, 7), we used a two-tailed *t*-test on spike counts binned in 400-ms windows (control versus photoinhibition). Spike counts from lick-right trials and lick-left trials were pooled. Spike rates were tested at different times during the task (in 50-ms time steps) and significance was reported for $P < 0.01$.

Quantification of the effects of perturbations on movement selectivity was complicated by the fact that ALM selectivity is coupled to upcoming movements. Grouping trials by the final movement (for example, using only correct lick-right trials) to compute selectivity would miss the trials in which photoinhibition caused the mice to switch future movements, thus underestimating the effects of photoinhibition on selectivity. We therefore used all trials (correct and incorrect) to compute selectivity when quantifying selectivity changes caused by photoinhibition (Figs 1, 2, 5 and Extended Data Figs 5, 7). Selectivity change was the selectivity difference between control and photoinhibition trials. To quantify the recovery time course of selectivity after photoinhibition, we looked for the first time bin when selectivity on photoinhibition trials reached 80% of the control selectivity (Figs 1g, 2e, 5e and Extended Data Figs 5, 7, green lines). Standard errors of the mean were obtained by bootstrap across neurons.

Analysis of population dynamics in the activity space. To analyse the relationship between ALM population activity and upcoming movements, we restricted analysis to the recording sessions from the bilateral photoinhibition experiments (Fig. 2) with >5 neurons recorded simultaneously for >5 trials per condition (16 out of 38 sessions, Figs 3, 4 and Extended Data Figs 6, 8, 9). For a population of n neurons, we found an $n \times 1$ vector, in the n dimensional activity space that maximally separated the response vectors in lick-right trials and lick-left trials, we term this vector the coding direction (CD).

Average spike counts were computed in a 400-ms window in 10-ms steps. For each movement direction (lick right and lick left, correct trials only) we computed the average spike counts $\bar{x}_{\text{lick right}}$ and $\bar{x}_{\text{lick left}}$, $n \times 1$ response vectors that described the population response at that time. During the sample and delay epochs the direction of the difference in the mean response vectors, $w_t = \bar{x}_{\text{lick right}} - \bar{x}_{\text{lick left}}$, was stable (correlation of w_t values between late sample epoch versus late delay epoch, 0.61 ± 0.05 ; Extended Data Fig. 9b). We averaged the w_t values from the sample and delay epochs to obtain the coding direction (CD). Because our estimate of the covariance was noisy, the CD gave better discrimination than the linear discriminant vector (CD divided by the within-group covariance).

The projection along the CD captured $65.6 \pm 5.1\%$ of the population selectivity for lick-left and lick-right trials over the sample and delay epochs (root mean square (r.m.s.) of the spike rate difference between lick-right trials and lick-left trials), and $36.4 \pm 6.3\%$ of the total variance in ALM task-related activity (Extended Data Fig. 8a). Activity variance was quantified as the r.m.s. of the baseline subtracted activity over the sample and delay epoch.

To project the ALM population activity along the CD we used independent control and perturbation trials from the trials used to compute the CD. For each trial we computed the spike counts for each neuron, x ($n \times 1$), at each time point. The projected trajectories in Figs 3, 5 and Extended Data Figs 6–9 were obtained as $CD^T x$. Both correct and incorrect trials were used to compute the projected trajectories, grouped by the instructed movements. To quantify the separation between trajectories on lick-right and lick-left trials, we computed ROC values using $CD^T x$ at the end of the delay epoch for each session. To average trajectories across multiple behavioural sessions (Figs 3, 5 and Extended Data Figs 7–9), we first offset the trajectories for a particular session by subtracting the mean $CD^T x$ across all trials and time points in that session. This removed fluctuations in mean activity from session to session. The offsets were computed using the independent control trials that were used to calculate the CD. Standard errors of the mean were obtained by bootstrapping individual sessions.

To predict upcoming movements using ALM responses projected onto the CD (Figs 3, 4 and Extended Data Figs 8b, 9), we used the response vector x from the last time bin before the go cue (last 400 ms of the delay epoch). For each session, we computed a decision boundary (DB) to best separate the projected responses, $CD^T x$, from lick-right and lick-left trials:

$$DB = \frac{CD^T x_{\text{lick right}} / \sigma_{\text{lick right}}^2 + CD^T x_{\text{lick left}} / \sigma_{\text{lick left}}^2}{1 / \sigma_{\text{lick right}}^2 + 1 / \sigma_{\text{lick left}}^2}$$

σ^2 is the variance of the projected responses $CD^T x$ across multiple lick-right or lick-left trials. Both the CD and decision boundary were computed using independent control trials and separate control and photoinhibition trials were used to predict performance. Data from multiple sessions were pooled in Figs 3, 4 and Extended Data Fig. 9.

We decomposed ALM activity into three forms of dynamics (Fig. 3 and Extended Data Fig. 8). The modes were computed using a subset of control trials (correct trials only) and ipsilateral perturbation trials. The projections in the figures are for independent control trials and perturbation trials. The projection along the CD (mode 1) captured the movement selectivity in activity. The persistent mode (mode 2) was the difference in the mean response vectors between ipsilateral perturbed and unperturbed lick-right trials at the go cue. Mode 3 was the mean response vectors between ipsilateral perturbed and unperturbed lick-left trials at the go cue, further rotated using Gram–Schmidt process to be orthogonal to mode 2. We did not orthogonalize the CD mode and persistent mode, so that any potential selectivity common to these modes was not removed. There was a small overlap between mode 1 and modes 2–3 (the activity variance and selectivity shared by modes 1–3 are quantified in Extended Data Fig. 8a). Modes 2 and 3 describe the vast majority of the persistent changes in activity after ipsilateral perturbations.

Two additional modes (4 and 5) captured the remaining activity variance. We first found eigenvectors of the population activity matrix using singular value decomposition. The data for the singular value decomposition (SVD) was an $n \times t$ matrix, consisting of the baseline-subtracted PSTHs for n neurons, with the lick-right and lick-left trials concatenated together (t time bins). The first two eigenvectors ($n \times 1$) were rotated using the Gram–Schmidt process to be orthogonal to modes 1–3, yielding modes 4 and 5. Modes 1–5 together explained $98.5 \pm 0.5\%$ of the total variance of task-related activity and $95.8 \pm 1.2\%$ of population selectivity over the sample and delay epochs. To predict upcoming movements using the projected responses on persistent mode and ramping mode (Fig. 3), we computed decision boundaries on the projected responses using the same procedures as for the CD mode.

Modelling and simulation. Model code can be found at <https://github.com/kpdaie/LiDaie>.

We constructed neural networks that have the ability to produce slow ramps of preparatory activity (Fig. 6a) when receiving transient or constant input, similar to a subset of ALM neurons. Our models include a phenomenological attractor model (Fig. 6b), explicit integrators (Fig. 6c and Extended Data Fig. 1f, g), and recurrent neural networks (RNNs) trained to produce ramping output (Fig. 6d and Extended Data Fig. 2h, i). We compared the responses of the models and ALM to transient silencing.

All networks were simulated for two seconds. Photoinhibition was simulated by holding the activity of half of the neurons in each network at zero for times $0.2 \text{ s} < t < 1.0 \text{ s}$. Activity of the i th neuron $r_i(t)$ was governed by the equation:

$$\frac{dr_i(t)}{dt} = -r_i(t) + \sum_{j=1}^N W_{i,j} f(r_j(t)) + I_i(t) + T_i(t) + \xi_i(t)$$

The cellular time constant, τ , the connectivity matrix, W , and the synaptic nonlinearity, $f(r)$, differed across the models. N is the number of neurons, $T_i(t)$ is a tonic and non-selective input, and $\xi_i(t)$ is Gaussian random noise. In all simulations networks received either transient ($0.05 \text{ s} < t < 0.1 \text{ s}$) or persistent ($0.1 \text{ s} < t < 1.9 \text{ s}$) sensory inputs $I_i(t)$.

Simple integrator model (Extended Data Fig. 1f). The network was simulated with $N=100$, $\tau=100 \text{ ms}$, and linear synapses, $f(r)=r$. The connectivity matrix was constructed so that all eigenvalues except for one were equal to zero. The non-zero eigenvalue was set to 0.99, producing feedback so that the activity of the network decays with time constant $\tau/(1-0.99)=10 \text{ s}$ (ref. 35). The input was either persistent (Extended Data Fig. 1f, left) or transient (Extended Data Fig. 1f, right), in which case the output from the integrator was cascaded into a second identical network to produce ramping activity. Silencing was simulated by holding the activity of a randomly-selected population of 50 neurons at zero for times $0.2 \text{ s} < t < 1.0 \text{ s}$.

Integrator with corrective feedback (Extended Data Fig. 1g). Corrective feedback³⁷ was incorporated into an integrator network to confer robustness against perturbations. The model consists of a pair of excitatory and inhibitory neurons. Corrective feedback was achieved by a mismatch in the time constants for excitatory and inhibitory connections, which generates negative derivative feedback. The network exhibits robustness against random perturbations that equally affect the excitatory and inhibitory neurons, but is not robust against asymmetric activation of inhibitory neurons (for example, photoinhibition). The function $f(r)$ is linear $f(r)=s$ where the auxiliary variable s is determined by the equation:

$$\tau_{\text{syn},i,j} \frac{ds_{i,j}}{dt} = -s_{i,j} + r_j(t)$$

The synaptic time constant $\tau_{\text{syn},i,j}$ determines how quickly the post-synaptic currents respond to changes in presynaptic activity. The synaptic time constants were: inhibitory synapses, 10 ms; excitatory to inhibitory neurons, 25 ms; excitatory to excitatory neurons, 100 ms. The network received a task-selective persistent input. Photoinhibition was simulated by injecting large currents into the inhibitory neuron and disallowing negative spike rates, which results in silencing of the excitatory neuron.

Trained RNN, FORCE learning (Extended Data Fig. 1h). We used FORCE²² training to minimize the difference between the network readout ($z(t)$) and a ramping waveform (Extended Data Fig. 1h). $z(t)$ is a linear combination of the activity of each neuron with weights determined by the vector w_0 (that is, $z(t)=\sum w_{0,j} r_j(t)$). Tuning of $z(t)$ was accomplished by simulating the activity of an initially randomly connected recurrent neural network (RNN) for 2 seconds (time step, 1 ms) and adjusting W every 2 ms during the simulation. This process was repeated 30 times.

The initial connectivity matrix was chosen to be sparse with a connection probability $p=0.1$. Non-zero connections were chosen from a Gaussian random distribution. The variance in connection strength was $\frac{1.5^2}{pN}$. 1.5 is a gain factor which is sufficiently strong to produce chaotic activity⁴⁹. In addition, we used $\tau=200 \text{ ms}$, $f(r)=\tanh(r)$, $N=400$ and transient input. Photoinhibition was simulated by transiently clamping the activity of a randomly-selected population of 200 (that is, $N/2$) neurons to zero. The network received either persistent (Extended Data Fig. 1h, left) or transient (Extended Data Fig. 1h, right) sensory input. For persistent input the network behaved similar to an integrator exhibiting a recovery of selectivity, albeit at an offset level upon removal of photoinhibition.

Trained RNN, tamed chaos (Extended Data Fig. 1i). RNNs were trained with FORCE as described above and further stabilized (tamed chaos)²³. The algorithm was designed to stabilize selected trajectories in chaotic networks via a recursive retuning of recurrent connection strengths based on a recursive least-squares rule⁵⁰. To minimize the number of synapses that required tuning, the FORCE network was made sparse by eliminating weak connections that were smaller than

an arbitrary threshold and using linear regression to adjust the remaining weights to maintain the dynamics. Elimination of weak synapses reduced the time needed to train the network. Twenty iterations of the tamed chaos algorithm were then run with weights being adjusted every 10 ms. Perturbations were applied as described for the FORCE trained network above. This training resulted in a modest increase in the robustness of the network.

Modular attractor (Fig. 6b). Two identical two-neuron unilateral attractor modules were constructed so that each neuron excited itself with weight 0.5235 and inhibited the other neuron in the same module with -0.5235 . Each neuron was reciprocally connected with one partner from the other module with strength 0.3.

$\tau=100 \text{ ms}$ and $f(r)=g(r)-g(0)$, where $g(r)=\frac{1.4}{1+e^{-(r-0.5)/0.3}}$. Transient input $I_i(t)$ (amplitude, 0.1) was provided to either the right-preferring (blue, Fig. 6b) or left-preferring (red, Fig. 6b) neurons, depending on the trial type. All neurons received a tonic input $T_i(t)$ with amplitude 0.5 and noise $\xi_i(t)$ with variance 0.01.

Modular integrator (Fig. 6c). Two modules with inter-module connections were tuned to produce robustness against unilateral photoinhibition. Each module consisted of four neurons (numbers refer to neuronal indices, with reference to the connection matrix W): Right preferring integrator neurons (1, 5) and left preferring integrator neurons (2, 6). Integration was produced by positive feedback achieved through mutual inhibition between left and right preferring neurons with strength -1 (ref. 15); these integrating pairs are represented schematically by the circles labelled J in Fig. 6c. The modules are connected through the recovery neurons (3, 7; 'R' in Fig. 6c) and gating inhibitory neurons (4, 8; 'G' in Fig. 6c). The input $I_i(t)$ was persistent with amplitude 0.04 to the right-preferring neuron and -0.04 to the left-preferring neuron during lick-right trials. The signs of the inputs were flipped for lick-left trials. In addition, each integrator neuron received tonic input $T_i(t)$ with amplitude 40.0 to produce baseline activity at 20.0.

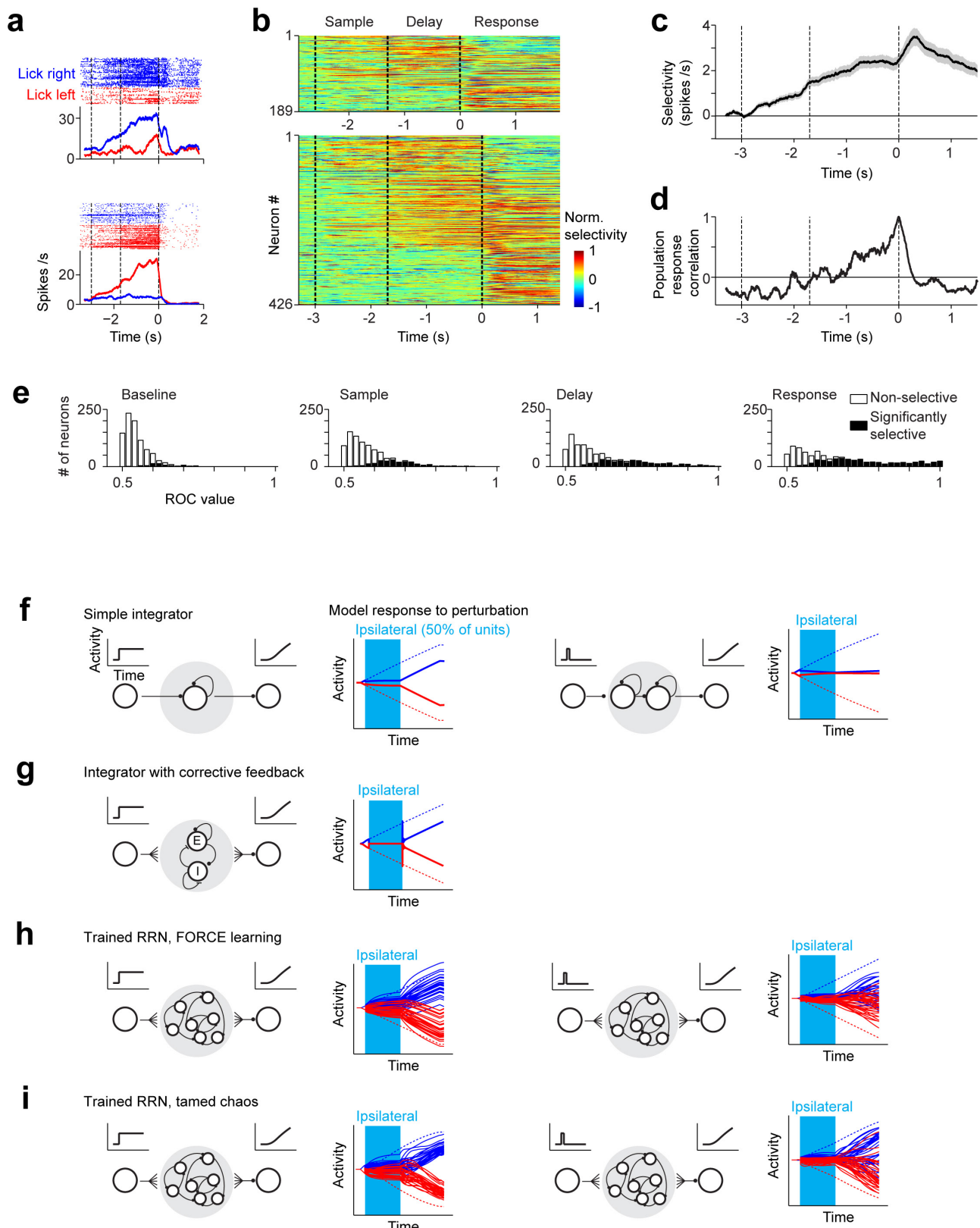
The recovery (Fig. 6c) and gating inhibitory (Fig. 6c) neurons together produce robustness. They receive positive input from the right-preferring neuron and negative input from the left-preferring neuron. After removal of photoinhibition, the recovery neuron restores the activity of the contralateral integrator neurons. This restorative connection has strength 0.5. To avoid excessive coupling between modules during normal function the recovery neuron is strongly inhibited by the gating neuron with strength -6.0 . The full connectivity matrix is shown below. For example, element $W_{1,7}$ is the connection from the recovery neuron in module 2 (neuron 7) onto the right preferring neuron of module 1 (neuron 1).

$$W = \begin{pmatrix} 0 & -1 & 0 & 0 & 0 & 0 & 0.5 & 0 \\ -1 & 0 & 0 & 0 & 0 & 0 & -0.5 & 0 \\ 1 & -1 & 0 & 0 & 0 & 0 & 0 & -6 \\ 1 & -1 & 0 & 0 & 0 & 0 & 0 & 0 \\ 0 & 0 & 0.5 & 0 & 0 & -1 & 0 & 0 \\ 0 & 0 & -0.5 & 0 & -1 & 0 & 0 & 0 \\ 0 & 0 & 0 & -6 & 1 & -1 & 0 & 0 \\ 0 & 0 & 0 & 0 & 1 & -1 & 0 & 0 \end{pmatrix}$$

The time constant of this network was $\tau=10 \text{ ms}$. Synapses in this network were linear, but activity was restricted to be positive. $\xi_i(t)=0$ in this network.

Modular tamed chaos (Fig. 6d). To generate a modular RNN we started, as above (see Trained RNN, FORCE learning), with a randomly connected RNN with $N=400$. We then classified 200 neurons as module 1 and the other 200 as module 2. FORCE training was performed as described above, but we first tuned only the intra-modular connections so that each module could produce its own ramping output. Next, inter-modular connections were trained in the presence of transient photoinhibition (described above) of module 1, so that the output of module 1 would recover upon removal of photoinhibition and the output of module 2 would be minimally affected by the photoinhibition. This process was then repeated for photoinhibition of module 2. In this network $T_i(t)=0$ and $\xi_i(t)=0$.

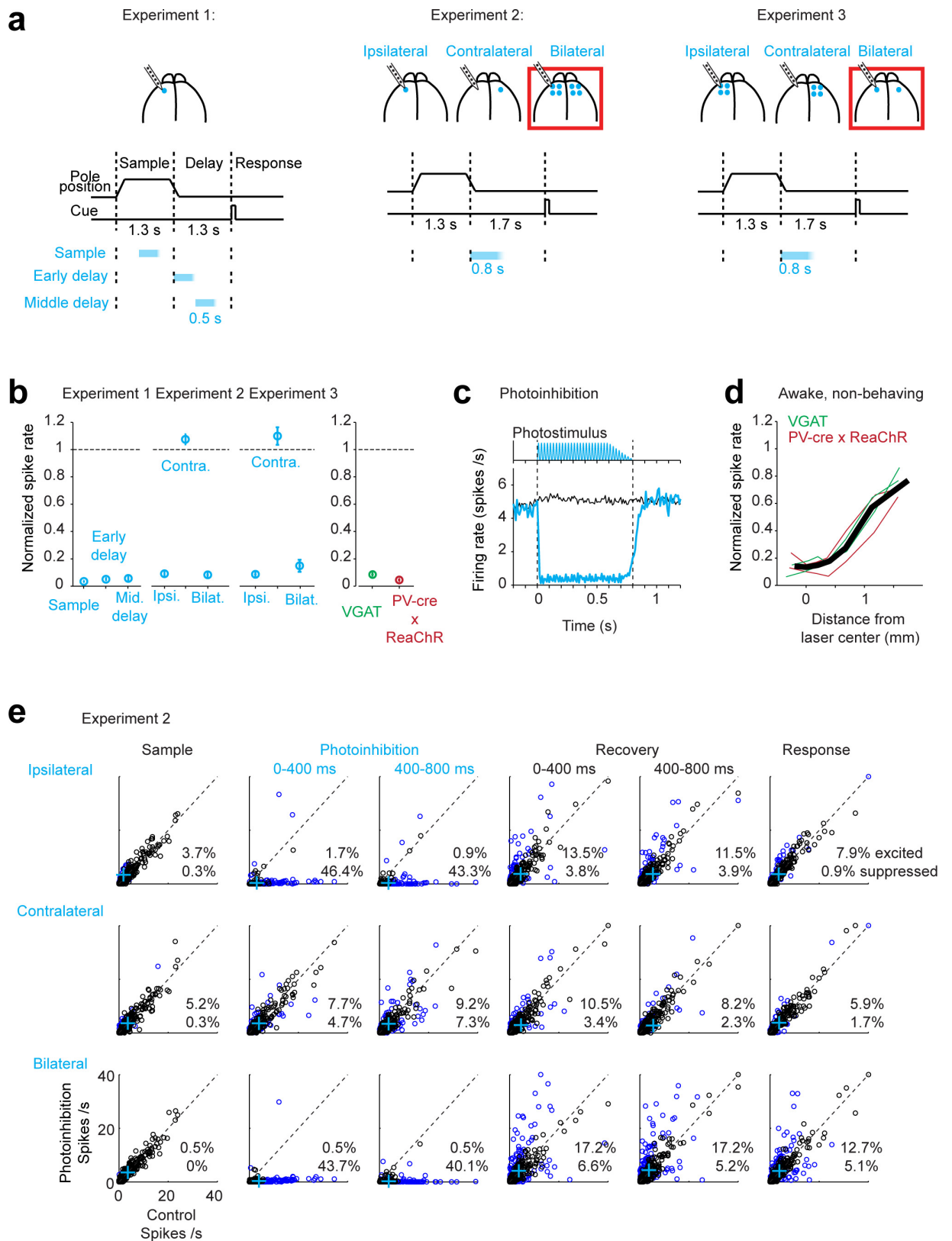
44. Hippnenmeyer, S. et al. A developmental switch in the response of DRG neurons to ETS transcription factor signaling. *PLoS Biol.* **3**, e159 (2005).
45. Hooks, B. M., Lin, J. Y., Guo, C. & Svoboda, K. Dual-channel circuit mapping reveals sensorimotor convergence in the primary motor cortex. *J. Neurosci.* **35**, 4418–4426 (2015).
46. Gerfen, C. R., Paletzki, R. & Heintz, N. GENSAT BAC cre-recombinase driver lines to study the functional organization of cerebral cortical and basal ganglia circuits. *Neuron* **80**, 1368–1383 (2013).
47. Madisen, L. et al. A toolbox of Cre-dependent optogenetic transgenic mice for light-induced activation and silencing. *Nature Neurosci.* **15**, 793–802 (2012).
48. Guo, Z. V. et al. Procedures for behavioral experiments in head-fixed mice. *PLoS ONE* **9**, e88678 (2014).
49. Sompolinsky, H., Crisanti, A. & Sommers, H. J. Chaos in random neural networks. *Phys. Rev. Lett.* **61**, 259–262 (1988).
50. Haykin, S. *Adaptive Filter Theory* 4th edn (Prentice Hall, 2002).



Extended Data Figure 1 | See next page for caption.

Extended Data Figure 1 | ALM activity during motor planning and network models of premotor dynamics. **a**, Two example ALM neurons with selectivity during the object location discrimination task, out of 890 putative pyramidal neurons from 12 mice (Methods). Correct lick-right (blue) and lick-left (red) trials only. Dashed lines demarcate behavioural epochs. Averaging window, 200 ms. **b**, ALM population selectivity. Top, delay epoch was 1.3 s; bottom, delay epoch was 1.7 s. Selectivity is the difference in spike rate between the preferred and non-preferred trial type, normalized to the peak selectivity (Methods). Only putative pyramidal neurons with significant trial selectivity are shown ($n = 634$ out of 890). In addition, neurons tested for <15 trials for each trial type (19 out of 634) were excluded. **c**, Average population selectivity in spike rate (black line, \pm s.e.m. across neurons, bootstrap). **d**, Population response correlation. Pearson's correlation between the population response vectors at different times during the task and the population response vector at

the onset of the go cue (time = 0). All selective putative pyramidal neurons were used, even if not recorded at the same time (ignoring potential correlations between neurons). To equalize the contributions of individual neurons, each neuron's response was mean-subtracted and normalized to the variance of its response across the entire trial (computed in time bins of 200 ms). **e**, Distribution of selectivity across the population during different epochs. For each neuron, a ROC value between lick-right and lick-left trials was computed using the spike counts during the particular behavioural epoch. Solid bars, neurons with significant trial-type selectivity ($P < 0.05$, two-tailed t -test using spike counts). **f-i** Monolithic models (see Methods). Each solid line represents the activity of the network's output in response to photoinhibition. Activity does not recover after transiently silencing subsets of neurons in: Simple integrator model³⁵ (**f**), Integrator with corrective feedback³⁷ (**g**), Trained RNN, FORCE learning²² (**h**), Trained RNN, Tamed Chaos²³ (**i**).

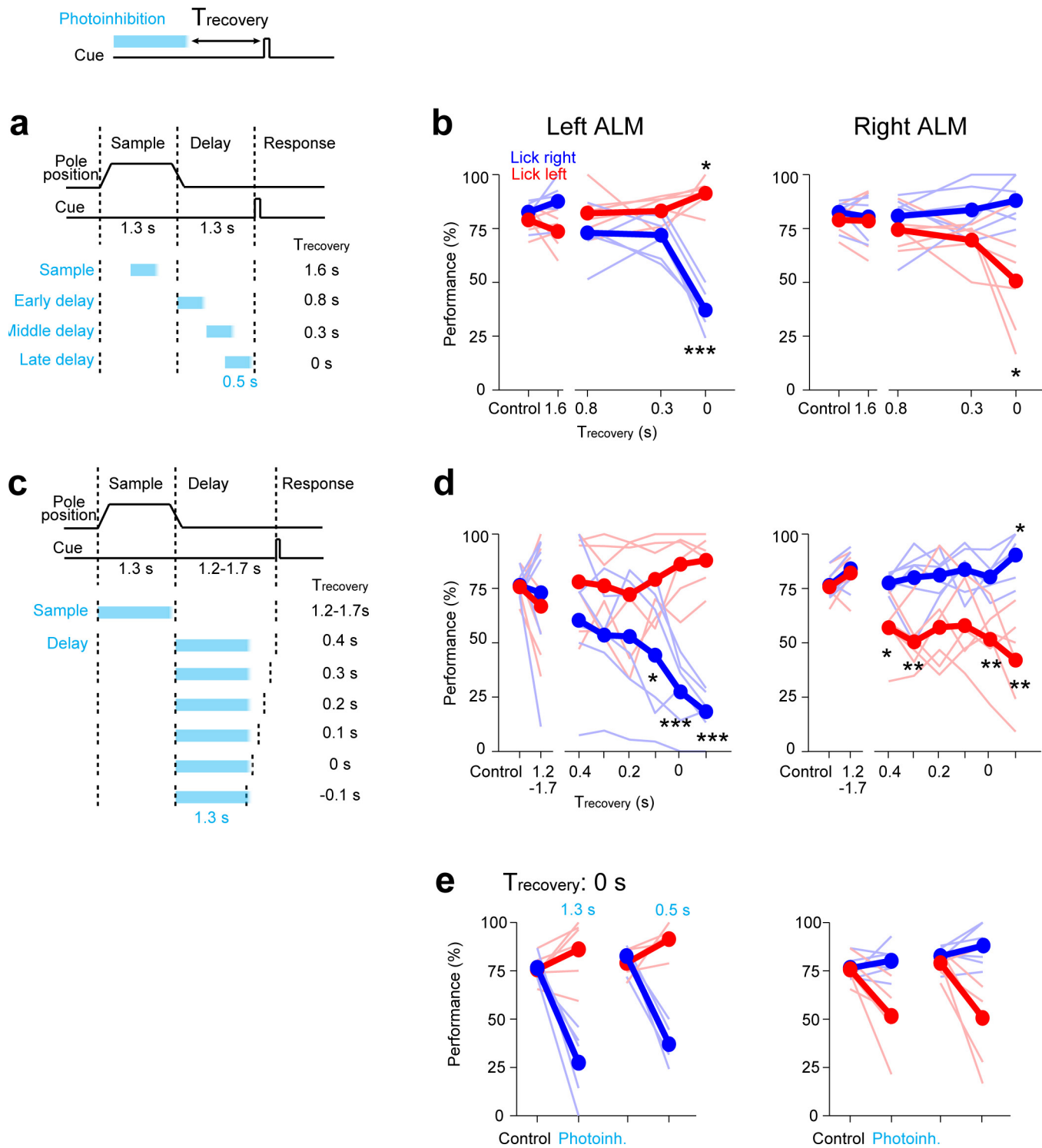


Extended Data Figure 2 | See next page for caption.

Extended Data Figure 2 | Characterization of photoinhibition.

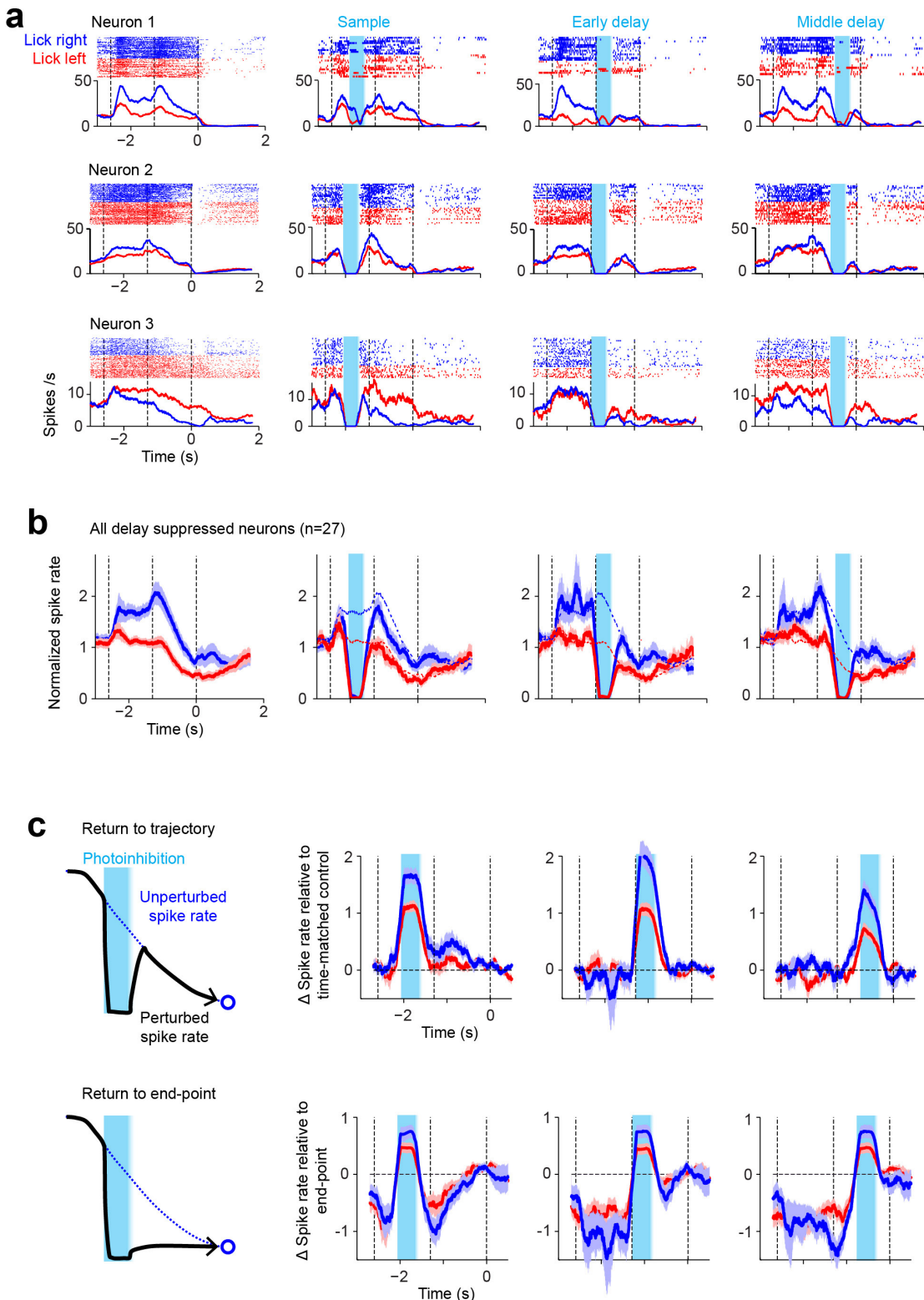
a, Silicon probe recording and photoinhibition in different experimental configurations used in this study. Experiment 1, data presented in Fig. 1 and Extended Data Figs 3, 4; experiment 2, data presented in Figs 2–4 and Extended Data Figs 6, 8, 9; experiment 3, data presented in Extended Data Fig. 7. **b**, Effect of photoinhibition on putative pyramidal neurons. For each neuron, spike rate during photoinhibition was normalized to spike rate in control trials. Left, experiment 1: $n = 117, 110$ and 109 neurons from 6 mice; experiment 2: $n = 300, 294$ and 301 from 7 mice; experiment 3: $n = 52, 52$ and 102 from 3 mice. Ipsilateral and bilateral photoinhibition similarly silenced neuronal activity. Average spike rate across the population was little affected by contralateral photoinhibition. Right, comparison of photoinhibition in VGAT-ChR2-EYFP mice and PV-ires-cre mice crossed to a ReaChR reporter line (Methods)⁴⁵. Photoinhibition was similar in the two mouse lines (>90% activity reduction). Data from ipsilateral photoinhibition from experiment 2 ($n = 94$ neurons from 3 VGAT mice; $n = 201$ from 4 PV-cre × ReaChR mice). Error bars, s.e.m. over neurons. Neurons with mean spike rate of <1 spikes s^{-1} were excluded. **c**, Top, photostimuli were shaped to minimize rebound activity after photoinhibition. Peak photostimulus intensity was gradually reduced over 200 ms during stimulus offset. Bottom, average spike rate across the population (black, control; cyan, photoinhibition). Data from experiment 2,

ipsilateral photoinhibition, $n = 300$ neurons from 7 mice. **d**, Effect of photoinhibition versus distance from the laser centre under the standard photostimulus (1 laser spot). Neurons were pooled across cortical depths. Recording data were obtained from ALM of 4 untrained mice under awake and non-behaving conditions. Recording procedures were described previously³. Thin lines, individual mice ($n = 246$ neurons, 2 VGAT-ChR2-EYFP mice, 2 PV-ires-cre × ReaChR mice). **e**, Average spike rates on control versus photoinhibition lick-right trials during different epochs of the task. Data from experiment 2. Photoinhibition was for 800 ms at the beginning of the delay epoch. The delay epoch was 1.7 s. Columns from left to right: the last 400 ms of the sample epoch, the first 400 ms of the photoinhibition, the last 400 ms of the photoinhibition, the first 400 ms after photoinhibition, 400 – 800 ms after photoinhibition, first 400 ms of the response epoch (see **a** for trial structure). Top, ipsilateral photoinhibition (1 laser spot, Methods); middle, contralateral photoinhibition (1 laser spot); bottom, bilateral photoinhibition (4 laser spots). Coloured dots, neurons with significant spike rate change ($P < 0.01$, two tailed t -test). Crosses, population means. No rebound excitation was detected after photoinhibition offset on average (**d**). A small proportion of neurons showed rebound excitation which was balanced by a low level of sustained inhibition in a larger proportion of neurons. Results are similar for lick-left trials (not shown).



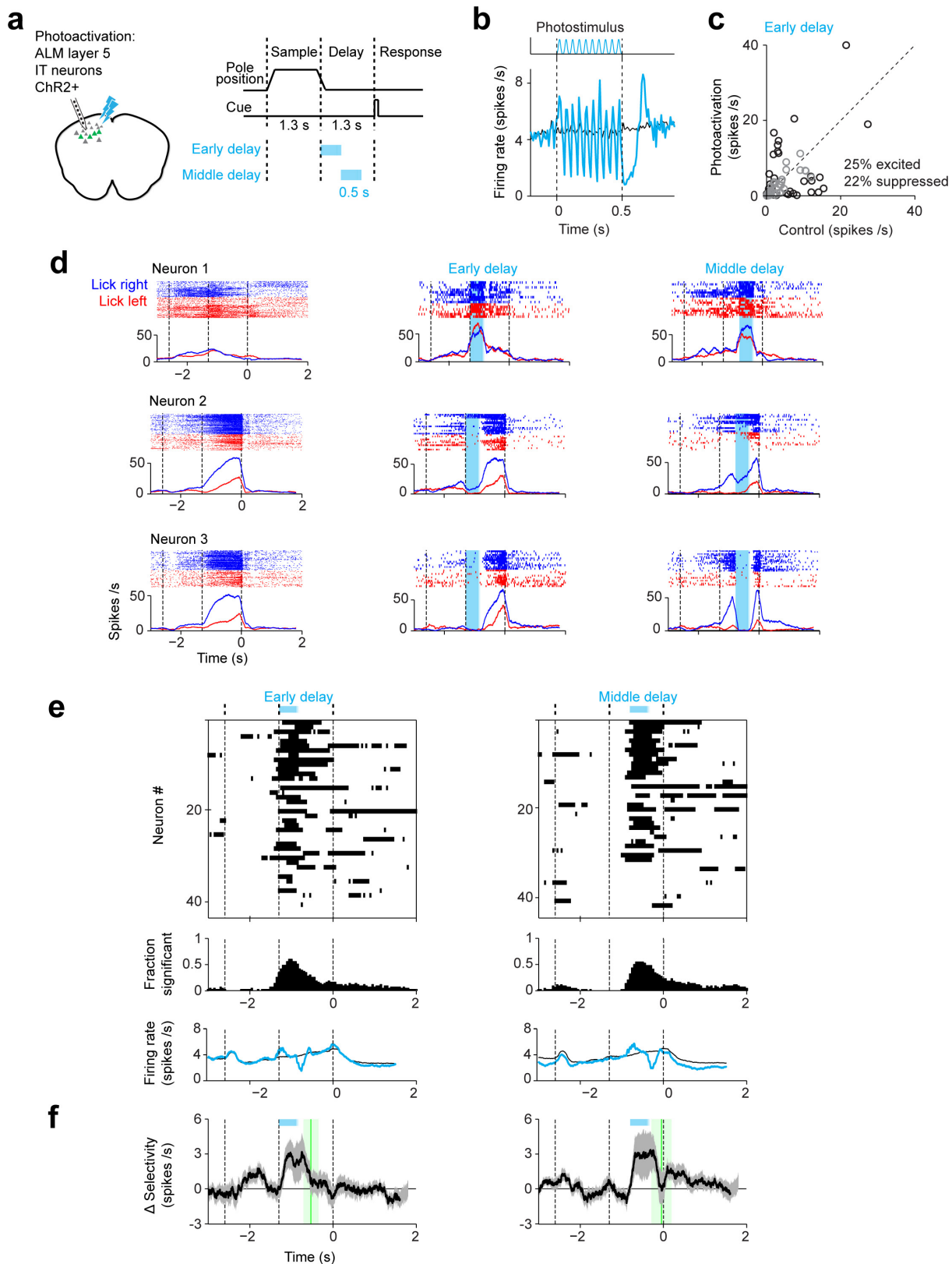
Extended Data Figure 3 | Unilateral photoinhibition of ALM immediately before movement causes ipsilateral bias. **a**, Unilateral photoinhibition of ALM during different task epochs. Sample epoch, 1.3 s; delay epoch, 1.3 s. Photoinhibition, 0.5 s (0.4 s and 0.1 s ramp, Methods). **b**, Performance with 0.5 s photoinhibition of left or right ALM during different trial epochs. Performance was plotted as a function of time interval between photoinhibition offset (the end of ramp offset) and the onset of go cue (T_{recovery}). Performance was not significantly affected for $T_{\text{recovery}} > 0.3$ s. Thick lines, mean; thin lines, individual mice ($n = 5$). * $P < 0.05$, ** $P < 0.01$, *** $P < 0.001$, two-tailed t -test.

c, Unilateral photoinhibition of ALM during different task epochs. Sample epoch, 1.3 s; delay epoch, variable duration, 1.2–1.7 s in 0.1-s increments. Trials with different delay epoch durations were randomly interleaved. Photoinhibition was for 1.3 s (1.2 s and 0.1 s ramp, Methods), resulting in different T_{recovery} . **d**, Performance with 1.3 s photoinhibition. Plot is similar to **b**. Performance was not significantly affected for $T_{\text{recovery}} > 0.3$ s. **e**, Photoinhibition (0.5 s) immediately before the go cue is similar to the behavioural effect caused by photoinhibition during the entire delay epoch (1.3 s). Photoinhibition data at $T_{\text{recovery}} = 0$ from **b** and **d** was re-plotted.



Extended Data Figure 4 | ALM neurons with decreasing spike rates during the delay epoch recovered their normal spike rates after unilateral photoinhibition. **a**, Three example ALM neurons with decreasing spike rates during the delay epoch. Top, spike raster. Bottom, PSTH. All lick-right (blue) and lick-left (red) trials. Dashed lines, behavioural epochs. Blue shades, photoinhibition. **b**, Normalized spike rate for all neurons with significant spike rate decrease at the end of the delay epoch compared to the beginning of the delay epoch ($P < 0.05$, two-tailed t -test; 400 ms windows; pooled across trial types). 27 neurons from 6 mice. The spike rate for each neuron was normalized to the mean spike rate. Blue, preferred trial type; red, non-preferred. Mean \pm s.e.m. across

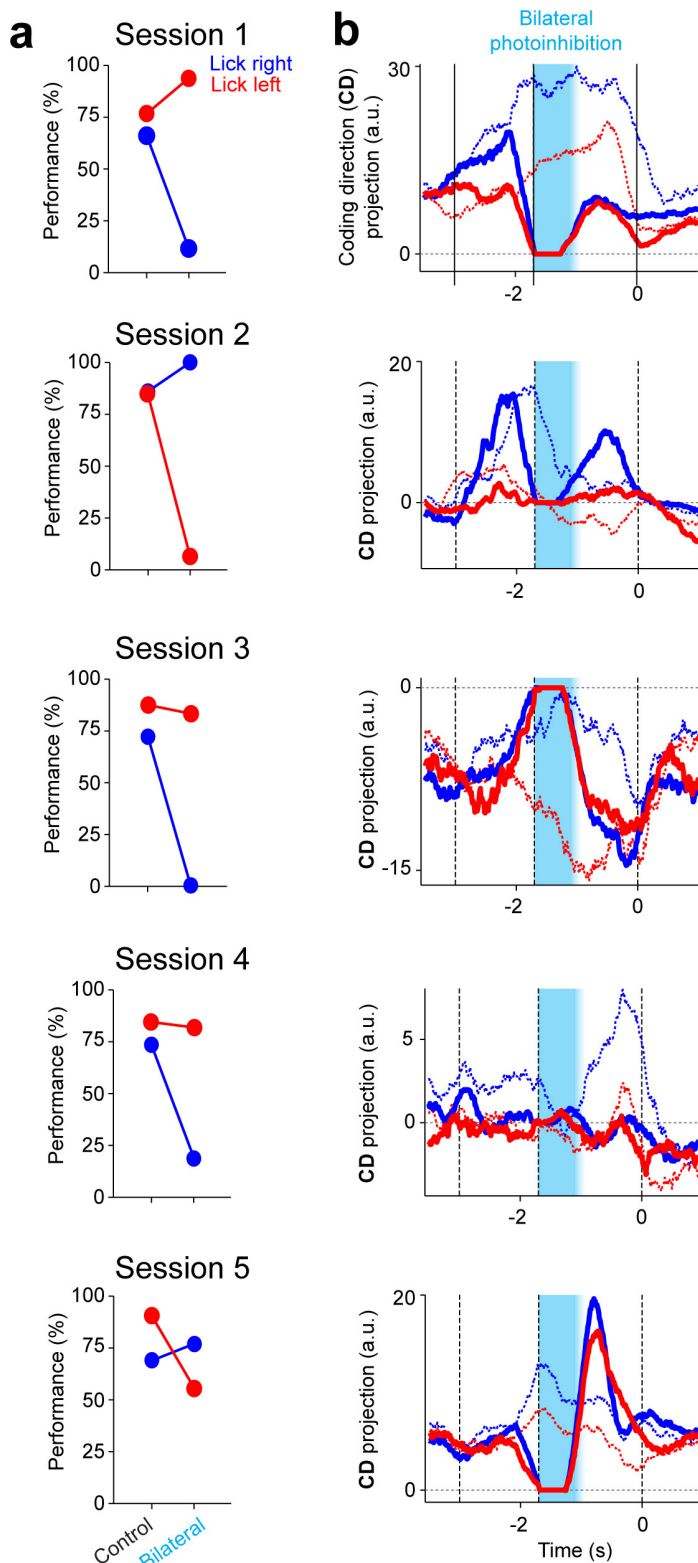
neurons, bootstrap. Dotted lines, spike rates in control trials. **c**, The data are consistent with a return to the normal trajectory and inconsistent with decay to the end point. Top, spike rate difference between perturbed trials and the time-matched spike rates in control trials. Bottom, spike rate difference between perturbed trials and the spike rates at the end of the delay epoch in control trials. Data from **b**. Mean \pm s.e.m. across neurons, bootstrap. Spike rate difference relative to time-matched control show significantly smaller root mean squared error (r.m.s.e.) than spike rate difference relative to end point ($P < 0.001$, paired t -test). r.m.s. was computed during the epoch between photoinhibition offset and the go cue.



Extended Data Figure 5 | See next page for caption.

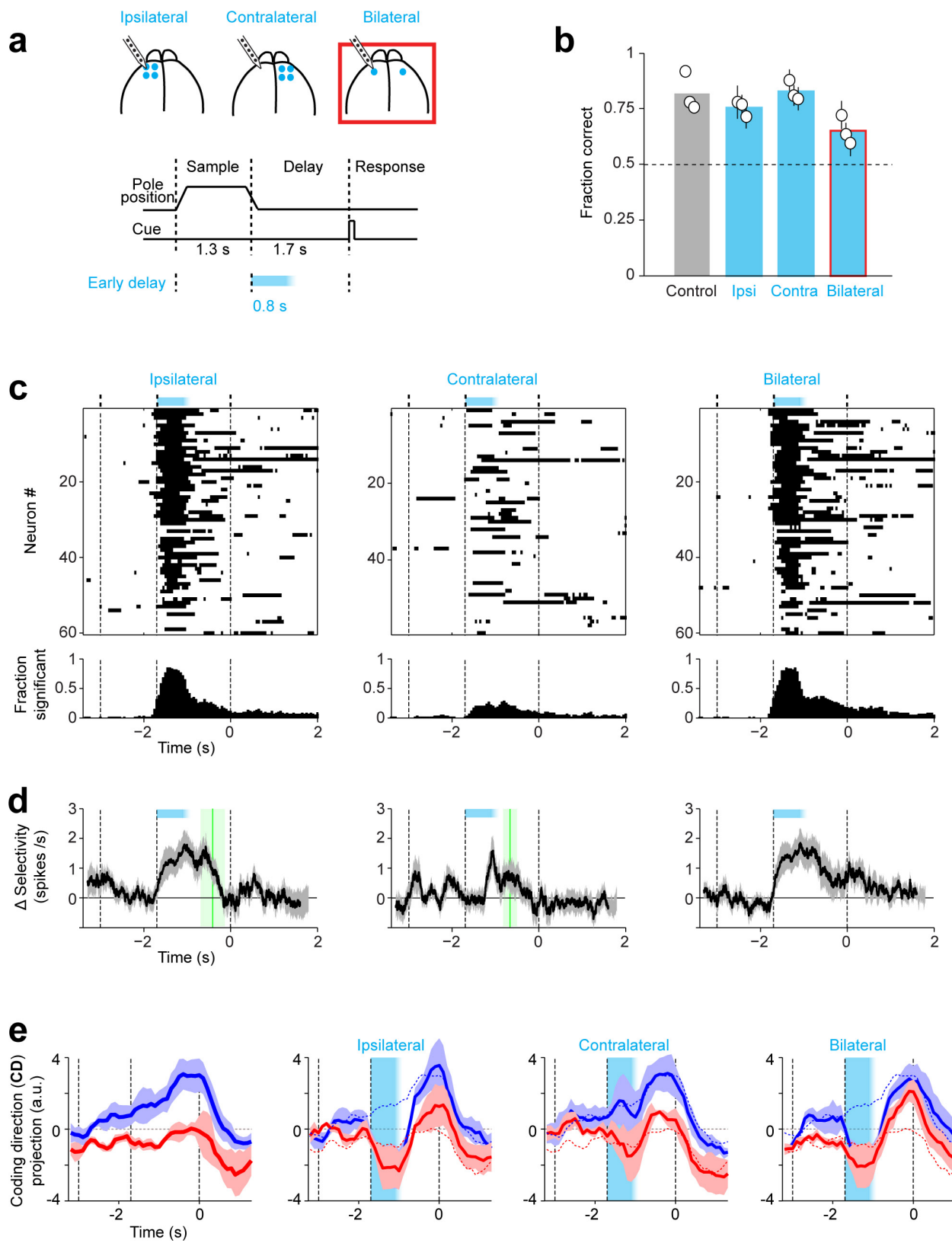
Extended Data Figure 5 | Preparatory activity is robust to photoactivation. **a**, Left, silicon probe recording during unilateral photoactivation of a subset of excitatory neurons. Tlx_PL56-Cre mice were crossed to Ai32 (Rosa26-ChR2) reporter mice to express ChR2 in layer 5 intratelencephalic (IT) neurons⁴⁶. Right, task structure and timing of photoactivation (cyan). **b**, Top, photostimulus. Bottom, average spike rate across the population ($n = 69$ neurons from 2 mice). Black, control; cyan, photoactivation. Rebound inhibition was observed after photoactivation. **c**, Effect of photoactivation on spike rates. Data are for photoactivation during early delay epoch. Black circles, neurons with significant spike rate change ($P < 0.01$, two tailed t -test). Photoactivation during sample epoch: 19% excited, 22% suppressed; late delay epoch: 15% excited, 17% suppressed. Lick-right and lick-left trials were pooled to compute spike rates. **d**, Three example ALM neurons. Top, spike raster. Bottom, PSTH.

All lick-right (blue) and lick-left (red) trials. Dashed lines, behavioural epochs. Blue shades, photoinhibition. **e**, Top, significant spike rate changes relative to control are highlighted for individual neurons. Neurons (rows) are sorted based on their mean spike rate across the trial epochs. Neurons with mean spike rate below 1 spikes s⁻¹ or tested for less than 3 trials are excluded. Middle, fraction of neurons with significant spike rate change ($n = 43, 44$ from 2 mice). Bottom, average spike rate across the population. **f**, Average population selectivity change from control (Δ selectivity \pm s.e.m. across neurons, bootstrap). Only selective neurons tested for >3 trials in all conditions are shown ($n = 26$). Green lines, time points when the selectivity recovered to 80% of control selectivity (mean \pm s.e.m. across neurons, bootstrap). Sample epoch: 249 \pm 68 ms to recover to 80% of control selectivity; early delay: 275 \pm 168 ms; middle delay: 250 \pm 218 ms.



Extended Data Figure 6 | ALM dynamics predicts upcoming movements at the level of behavioural sessions. **a**, Behavioural performance on control and bilateral photoinhibition trials. **b**, Time course of activity trajectories projected onto the coding direction (CD). Dotted lines, average trajectories from control lick-right (blue) and lick-left (red) trials. Solid lines, average trajectories from bilateral photoinhibition trials. Each plot shows data from one session for one mouse. Trajectories in photoinhibition trials were similar to control trials before photoinhibition and were persistently altered by transient bilateral photoinhibition. The resultant trajectories were inconsistent from session

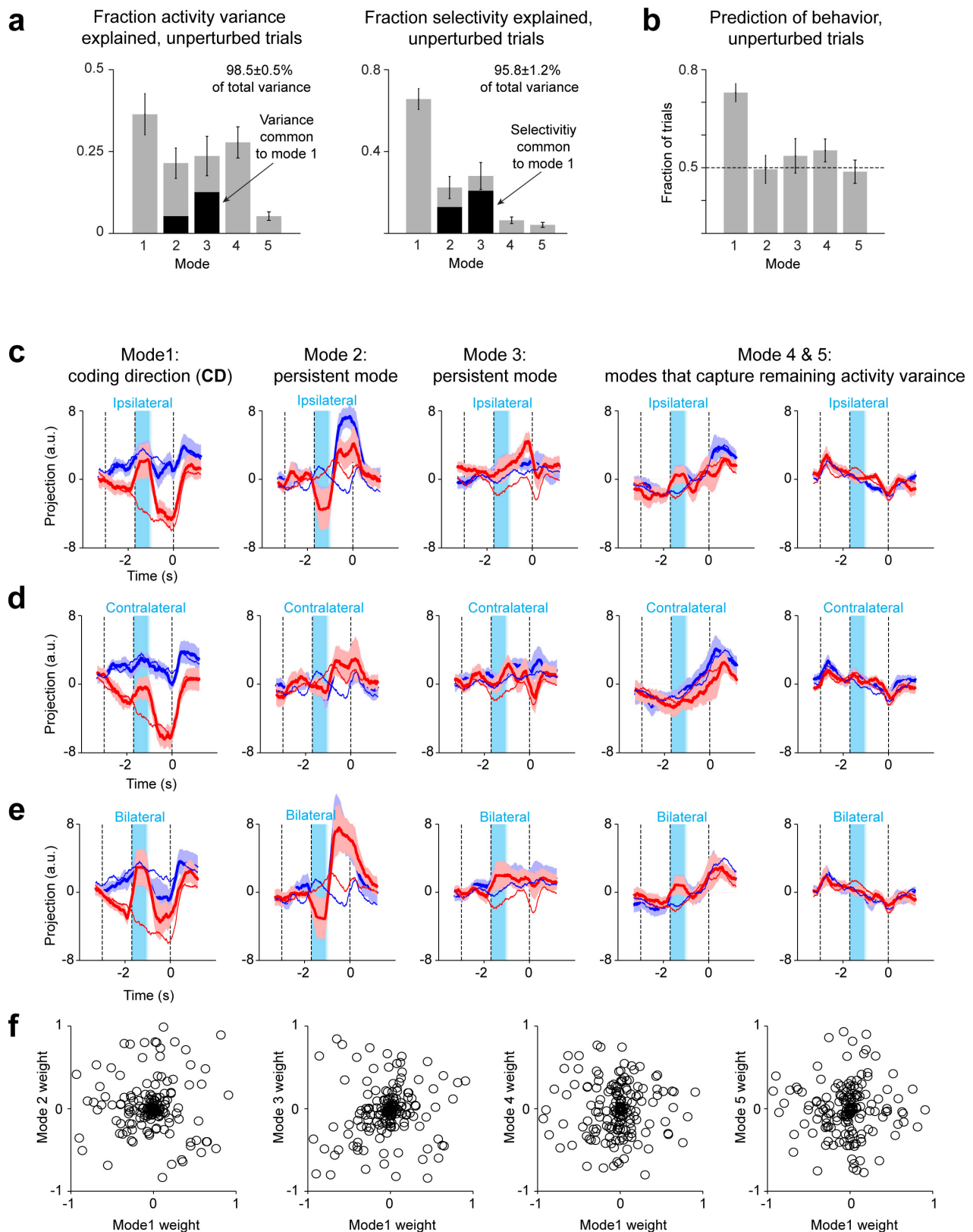
to session: in some cases the altered trajectories were closer to the lick-right control trajectories (blue dotted lines), and in other cases closer to the lick-left control trajectories (red dotted lines). Averaging window, 400 ms. In sessions with altered activity trajectories that were closer to the control lick-left trajectories, movements were biased to the left, resulting in high performance in lick-left trials and low performance in lick-right trials (session 1, 3, 4). The opposite behavioural bias was observed when altered activity trajectories were closer to the control lick-right trajectories (session 2, 5). The biases in movement were predicted based ALM activity trajectories. Session 1–5, $n = 20, 16, 18, 10$ and 12 neurons.



Extended Data Figure 7 | See next page for caption.

Extended Data Figure 7 | Bilateral photoinhibition disrupts ALM dynamics and behaviour. **a**, Silicon probe recording during unilateral (4 laser spots) and bilateral (1 laser spot; red box) photoinhibition. **b**, Behavioural performance. Bar, mean across all mice ($n=3$). Symbols, individual mice (mean \pm s.e.m., bootstrap). **c**, Top, significant spike rate changes for individual neurons (black). Neurons (rows) are sorted based on their mean spike rate across the trial epochs. Neurons with mean spike rate below 1 spike s^{-1} or tested for less than 3 trials are excluded ($n=60$, 59 and 60). Photoinhibition is indicated on the top. Bottom, fraction of neurons with significant spike rate change. **d**, Average population selectivity change from control (Δ selectivity \pm s.e.m. across neurons, bootstrap). Only selective neurons tested for >3 trials in all conditions are shown ($n=40$). Green lines, time points when the selectivity recovered to 80% of control selectivity (mean \pm s.e.m. across neurons, bootstrap).

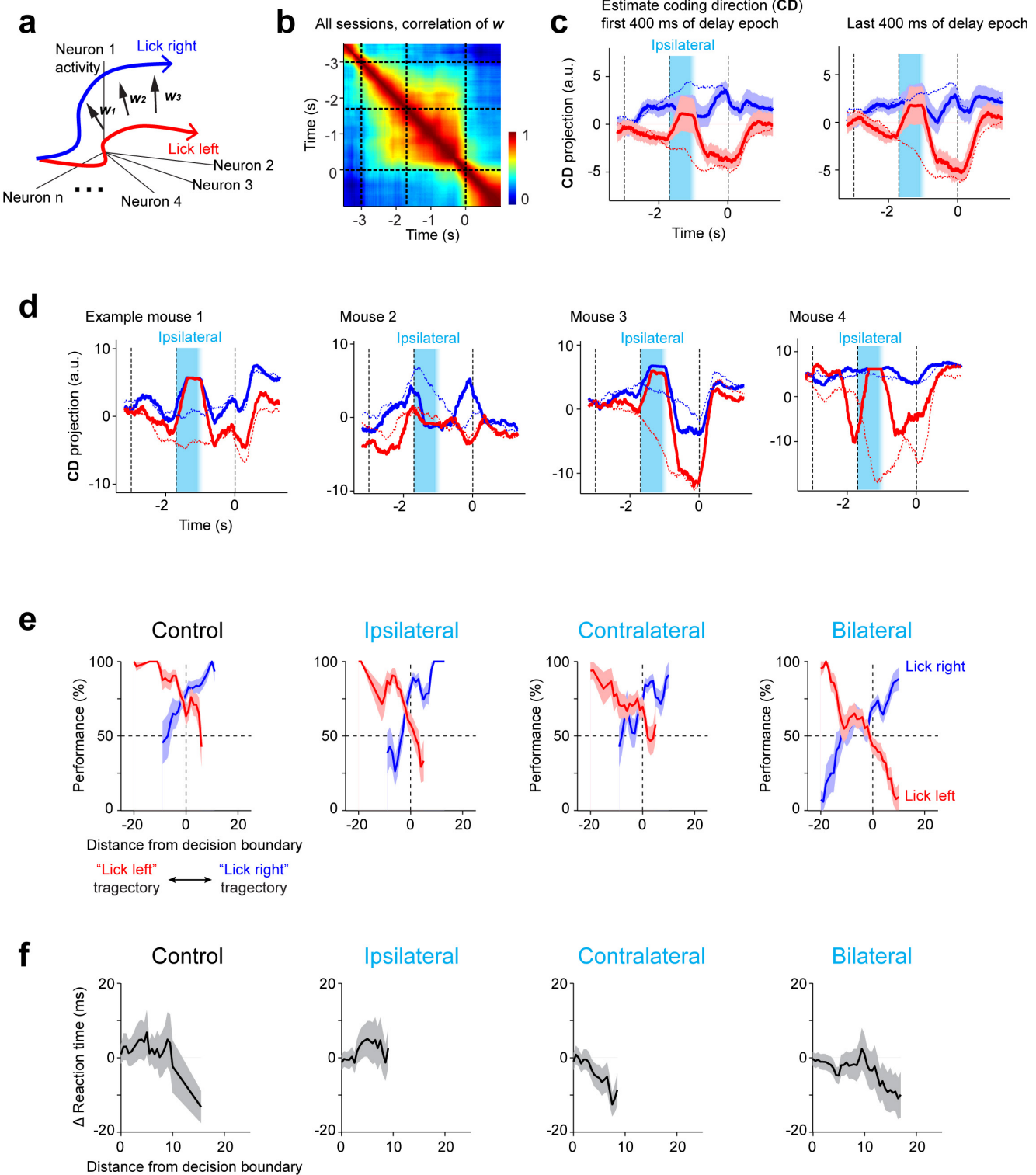
Ipsilateral: 490 ± 280 ms to recover to 80% of control selectivity; contralateral: 235 ± 156 ms; bilateral: no recovery at end of delay period. **e**, Time course of activity trajectories on lick-right (blue) and lick-left (red) trials projected onto the coding direction (CD). Average trajectories from all sessions (\pm s.e.m. across sessions, bootstrap, Methods). From left to right panels: control trials, ipsilateral photoinhibition (4 laser spots), contralateral photoinhibition (4 laser spots), and bilateral photoinhibition (1 laser spot). Dotted line, trajectories in control trials. Only sessions with >5 simultaneously recorded neurons tested for >3 trials in each condition. We quantified the separation between trajectories at the end of delay epoch by computing ROC values for each session: control, 0.80 ± 0.08 ; ipsilateral, 0.64 ± 0.10 ; contralateral, 0.68 ± 0.15 ; bilateral, 0.54 ± 0.8 . Mean \pm s.e.m. across sessions, Methods.



Extended Data Figure 8 | See next page for caption.

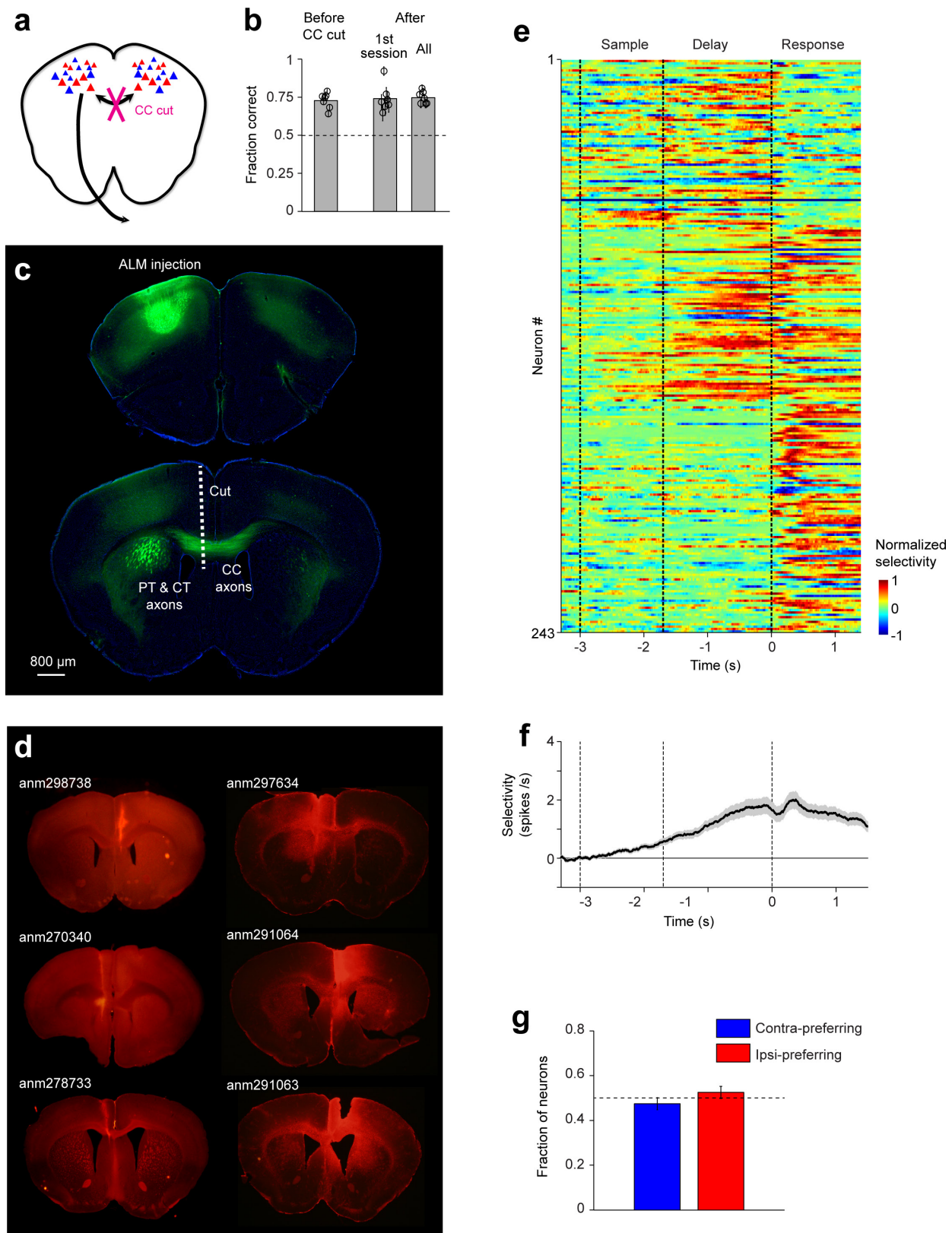
Extended Data Figure 8 | Decomposition of ALM dynamics after perturbation. **a**, Decomposition of activity into five modes based on control trials and ipsilateral perturbations (Methods). Fraction of activity variance (left) and selectivity (right) explained by modes 1–5. The overlap in variance and selectivity between mode 1 and modes 2–3 are highlighted in black. Error bars, s.e.m. across sessions. Data from 16 sessions, 7 mice. Activity variance here is computed using trial-averaged activity (Methods), thus they reflect variance across time and neurons. Activity variance across trials is not reflected. The fraction of variance explained for the single-trial activity would be much lower. **b**, Fraction of upcoming movements predicted based on modes 1–5. Trajectory distance from the decision boundary at the time of the go cue is used to predict behaviour. Lick-right and lick-left trials are pooled. Error bars, s.e.m. across sessions. **c**, Projections of activity along modes 1–5 for ipsilateral perturbation trials (solid). Dashed blue and red lines correspond to the means for control

trials. Error bars, s.e.m. across sessions. For the **CD** mode, a different set of trials was used here to compute **CD** compared to Fig. 3c (Methods). This resulted in small differences in the projected trajectories. **d**, Projections of activity in the same dimensions as in **c** for contralateral perturbation trials. **e**, Projections of activity in the same dimensions as in **c** for bilateral perturbation trials. **f**, Weights of each neuron for mode 1 versus modes 2–5. Mode 1 and modes 2–5 involve overlapping populations of neurons. Data from all sessions were pooled. Note that the ramping modes (4 and 5) are resistant to all perturbations, including bilateral perturbations, suggesting that overall ramping may be driven by a source external to ALM. ROC values between trajectories along the **CD** mode at the end of delay epoch: control, 0.76 ± 0.03 ; ipsilateral, 0.73 ± 0.02 ; contralateral, 0.74 ± 0.03 ; bilateral 0.58 ± 0.03 . ROC values during the time period of photoinhibition: control, 0.72 ± 0.02 ; ipsilateral, 0.54 ± 0.03 ; contralateral, 0.64 ± 0.03 ; bilateral 0.54 ± 0.01 .



Extended Data Figure 9 | ALM dynamics along the coding direction predicts upcoming movements. **a**, Schematic of trajectory analysis in activity space. The difference in the mean response vectors between lick-right and lick-left trials, w , was estimated across different time windows (400 ms) during sample and delay epochs. **b**, w values are similar during sample and delay epoch. Correlation of w values across time. Data from 16 sessions, 7 mice. The coding direction (CD) was taken as the average w value over time. **c**, The recovery of ALM dynamics along the coding direction (CD) is robust to the choice of time window for the calculation of CD. Left, CD was the average w value from the first 400 ms of the delay epoch. Right, CD was the average w value from the last 400 ms of the delay epoch. **d**, The recovery of ALM dynamics along CD is robust across mice.

e, Behavioural performance in lick-right and lick-left trials as a function of trajectory distance from the decision boundary at the time of the go cue. Positive values on the x axis indicate closer distance to the control lick-right trajectory. From left to right panels: control trials, ipsilateral photoinhibition trials, contralateral photoinhibition trials, and bilateral photoinhibition trials. Performance was computed by binning along the CD distance (bin size, 4 on the CD distance scale). s.e.m. was obtained by bootstrapping the trials in each bin. **f**, Reaction times are faster on trials in which the trajectory is far from the decision boundary at the time of the go cue. Δ Reaction time is relative to the mean reaction time from each session. Data from 16 sessions, 7 mice. Data from lick-right and lick-left trials were pooled.



Extended Data Figure 10 | See next page for caption.

Extended Data Figure 10 | Behavioural and ALM dynamics after corpus callosum hemisection. **a**, Schematic. Corpus callosum (CC) was bisected while sparing the pyramidal tract (PT) and corticothalamic (CT) projections. **b**, Behavioural performance. Bar, mean across all mice ($n=7$). Symbols, individual mice (mean \pm s.e.m., bootstrap). Performance was not affected by the corpus callosum bisection. First session was ~ 17 h after the corpus callosum bisection. **c**, Location of the corpus callosum cut superimposed on axonal projections from ALM. AAV2/1-CAG-EGFP was injected into ALM. A vertical cut ~ 3.5 mm deep was made approximately 0.5 mm from the mid-line. The cut extended from bregma anterior 1.5 mm to posterior 1 mm. The cut was either made in the left hemisphere (3 mice) or the right hemisphere (4 mice). The cut spared the

pyramidal tract and corticothalamic axons. **d**, Coronal section showing the corpus callosum bisection in 6 mice. Left, autofluorescence; right, GFAP immunofluorescence (Methods). **e**, ALM shows normal preparatory activity after the corpus callosum bisection. ALM population selectivity. Selectivity is the difference in spike rate between the preferred and non-preferred trial type, normalized to the peak selectivity (Methods). Only putative pyramidal neurons with significant trial selectivity are shown ($n=254$ out of 496). In addition, 11 out of 254 neurons tested for <15 trials for each trial type were excluded. **f**, Average population selectivity in spike rate (black line, \pm s.e.m. across neurons, bootstrap). **g**, Proportion of contra-preferring vs. ipsi-preferring neurons. Error bars, s.e.m. across mice, bootstrap.

CORRECTIONS & AMENDMENTS

CORRIGENDUM

doi:10.1038/nature18623

Corrigendum: Robust neuronal dynamics in premotor cortex during motor planning

Nuo Li, Kayvon Daie, Karel Svoboda & Shaul Druckmann

Nature **532**, 459–464 (2016); doi:10.1038/nature17643

We would like to correct several minor errors in this Article. In the Fig. 2b legend, ‘ $*P < 0.01$ ’ should have read ‘ $**P < 0.01$ ’. In the Methods ‘Photoinhibition’ section, the description of galvo step time during photoinhibition of multiple cortical locations should have read ‘step time: <0.2 ms; dwell time: >4.8 ms’ instead of ‘step time: <4.8 ms;’. In Extended Data Fig. 4c, the y -axis values of the three bottom panels should have run from -1 to 1 , instead of from 0 to 2 . In the Extended Data Fig. 5a legend, the citation given for Tlx_PL56-Cre mice should have been to ref. 46, rather than ref. 50. In the Extended Data Fig. 6b legend, the sessions were incorrectly referred to as ‘lick-right trials (session 1, 4)’ and ‘control lick-right trajectories (session 2, 3, 5)’ instead of ‘lick-right trials (session 1, 3, 4)’ and ‘lick-right trajectories (session 2, 5)’. All of these errors have been corrected online, and none of them affects the description, interpretation or conclusions of the Article.